Quantitative analysis of lattice disorder and crystallite size in organic semiconductor thin films

Jonathan Rivnay,[1] Rodrigo Noriega,[2] R. Joseph Kline,[3] Alberto Salleo,[1] and Michael F. Toney[4]

[1]*Materials Science and Engineering, Stanford University, Stanford, California 94305, USA*
[2]*Applied Physics, Stanford University, Stanford, California 94305, USA*
[3]*National Institute for Standards and Technology, Gaithersburg, Maryland 20899, USA*
[4]*Stanford Synchrotron Radiation Lightsource, SLAC National Accelerator Laboratory, Menlo Park, California 94025, USA*

The crystallite size and cumulative lattice disorder of three prototypical, high-performing organic semiconducting materials are investigated using a Fourier-transform peak shape analysis routine based on the method of Warren and Averbach (WA). A thorough incorporation of error propagation throughout the multistep analysis and a weighted fitting of Fourier-transformed data to the WA model allows for more accurate results than typically obtained and for determination of confidence bounds. We compare results obtained when assuming two types of column-length distributions, and discuss the benefits of each model in terms of simplicity and accuracy. For strongly disordered materials, the determination of a crystallite size is greatly hindered because disorder dominates the coherence length, not finite size. A simple analysis based on trends of peak widths and Lorentzian components of pseudo-Voigt line shapes as a function of diffraction order is also discussed as an approach to more easily and qualitatively assess the amount and type of disorder present in a sample. While applied directly to organic systems, this methodology is general for the accurate deconvolution of crystalline size and lattice disorder for any material investigated with diffraction techniques.

I. INTRODUCTION

While it is often convenient to describe crystalline matter as perfectly periodic, the true nature of most crystalline materials, especially weakly bonded solids such as organic materials, is unmistakably highly defective.[1] The presence of defects and disorder will disrupt the spatial and energetic periodicity of the material, and can have a large effect on electronic and optical functionality, as well as on thermal and mechanical properties. For example, direct connections have been made between intracrystalline lattice disorder and the mechanical properties of Kevlar fibers.[2] Optoelectronic materials, on the other hand, rely on the overlap of initially localized molecular wavefunctions to exhibit their optimal properties. Molecular orbital overlap in organic molecules is thus highly dependent on the relative spacing and orientation between adjacent molecules.[3] Thus, it is reasonable to expect that static statistical fluctuation in crystalline order will affect electronic transport and charge-trapping properties of conducting and semiconducting materials.[4] Such effects will be particularly significant in materials prone to distortions, e.g., the van der Waals bonded organic semiconductors described herein. Consequently, the understanding and quantification of lattice disorder and defects is of great importance for designing and engineering improved materials.

Diffraction line-shape analysis has been known to provide information about the general disorder and finite size of the crystalline domains. At the simplest level, one commonly used approach in the analysis of atomic and molecular solids is to determine the approximate size of crystalline grains from the breadth of x-ray-diffraction peaks using the Scherrer equation,[5,6] which relates the peak width and the coherence length (L_c):

$$L_c = \frac{2\pi K}{\Delta_q}, \tag{1}$$

where K is a shape factor (typically 0.8–1), and Δ_q is the full width at half the maximum of a diffraction peak. The scattering vector is $q = (4\pi/\lambda)\sin(\theta)$ for a given scattering angle 2θ and x-ray wavelength λ.

This approach is often used because it is easy to apply, involves minimal data processing, and can often give descriptive evidence for relative changes when processing conditions are varied experimentally. Because of its simplicity however, this equation lends itself to misuse. Besides the shape factor, which can be a source of considerable debate, and assumptions about grain size distribution, the Scherrer equation in Eq. (1) assumes that the crystallite size is the main contributor to the broadening of diffraction peaks: lattice disorder is ignored. As disorder becomes non-negligible, it is necessary to consider this contribution to the observed line shape.

Lattice disorder is manifest in a number of forms and has largely been ignored in the analysis of thin films, especially those of organic semiconductors. Lattice disorder can be manifest in two forms: noncumulative and cumulative disorder. *Noncumulative disorder* (historically termed disorder of the first kind) is characterized by random statistical fluctuations about an ideal lattice position, where the average lattice is preserved. Thermal fluctuations generally fall into this category, but frozen local defects and strain fluctuations giving rise to noncumulative disorder can occur as well. Noncumulative disorder is characterized by a lowering of the peak intensity,[5] which does not affect the peak shape and breadth and thus does not affect the analysis described herein. A detailed account of this type of disorder is beyond the scope of this work. *Cumulative disorder* (or disorder of the second kind) describes the statistically homogeneous disturbances to an ideal crystalline lattice which produce long-range distortion. To represent this type of disorder, the periodic lattice vectors are replaced with vectors of statistically determined magnitude and directions, whose deviations from ideal are described by

probability functions. Cumulative disorder dictates that the local arrangements of atoms have slight disturbances from the average but with no memory of the arrangements in another part of the crystalline domain (Fig. 1). This means that if we were to monitor the separation between two points in the lattice, r_i and r_j, the deviation from ideal positions would be a function of the separation

$$\Delta \vec{r}_{ij} = \vec{r}_j - \vec{r}_i = \Delta \vec{r}_{ij}\,|_{\text{ideal}} + \delta \vec{r}(\vec{r}_j - \vec{r}_i), \qquad (2)$$

while in the case of noncumulative disorder, the deviation from ideality δr is independent of the magnitude of the vector describing their separation (for large enough separation), although it may depend on its direction. In this work we focus on the main contribution of cumulative disorder, termed paracrystalline disorder. The concept of paracrystallinity was first pioneered by Hosemann[2,7] and is described in detail in the literature.[1,8,9] A measure of the statistical fluctuation of individual lattice spacings, the paracrystallinity parameter g, is commonly reported as a percent of the mean lattice spacing. Real materials typically exhibit paracrystalline disorder in the range of 0–15%, where <1% represents highly crystalline material, 1–10% represents paracrystalline material, and 10–15% represents a glass or melt.[2]

Cumulative lattice disorder can arise from dislocations, impurities, chain backbone twists (in polymers), or nonideal packing (in small molecule, weakly bonded solids). While the specific cause can rarely be distinguished by peak-shape analysis, the end result is disorder characterized by compounding, cumulative distortions. Regardless of its origins, cumulative disorder can be decoupled from the effects of finite crystallite size by the distinct broadening of higher-order diffraction peaks.

While both cumulative and noncumulative disorder can coexist (as in the case of thermal fluctuations about an already distorted paracrystalline lattice), Takahashi postulated that inter-crystalline variation in average lattice spacing can also be deconvoluted from the diffraction line shape, as it too has a dependence on diffraction order.[10] This phenomenon is termed lattice-parameter fluctuation, or nonuniform strain (e_{rms}). Lattice-parameter fluctuation describes the variance of the interplanar spacing within a sample—from one crystallite to the next, from one area of the diffracting volume to another—thus characterizing slight inhomogeneities within a sample. Examples include a slight contraction or expansion of the lattice spacings due to interfaces, a swelling of the outer regions of a grain due to impurities or solvents at grain boundaries or strains created by solvent evaporation. Nevertheless, it is clear that in all real crystals some amount of disorder exists. Quantifying such disorder is therefore of great importance to further our understanding of structure-property relationships.

Approaches to line-shape analysis rely on the fact that finite crystallite size affects peak breadth but is independent of diffraction order, while other terms cause a progressive broadening of the higher-order diffraction peaks [e.g., (200),(300),...,(m00)]. Additionally, the functional form with which peaks broaden can be attributed to different types of disorder or defects.[11] Thus, for example, by plotting the peak breadth vs diffraction order, one can extract the grain size from the intercept ($m = 0$), while the functional form of the broadening [i.e., $\Delta_q(m)$] can reveal the mechanism and magnitude of the lattice nonidealities.[11–13] This approach, classified as an integral breadth method (related to the analysis of Williamson and Hall),[14,15] is useful in strongly diffracting materials, but it is difficult to reliably determine the appropriate
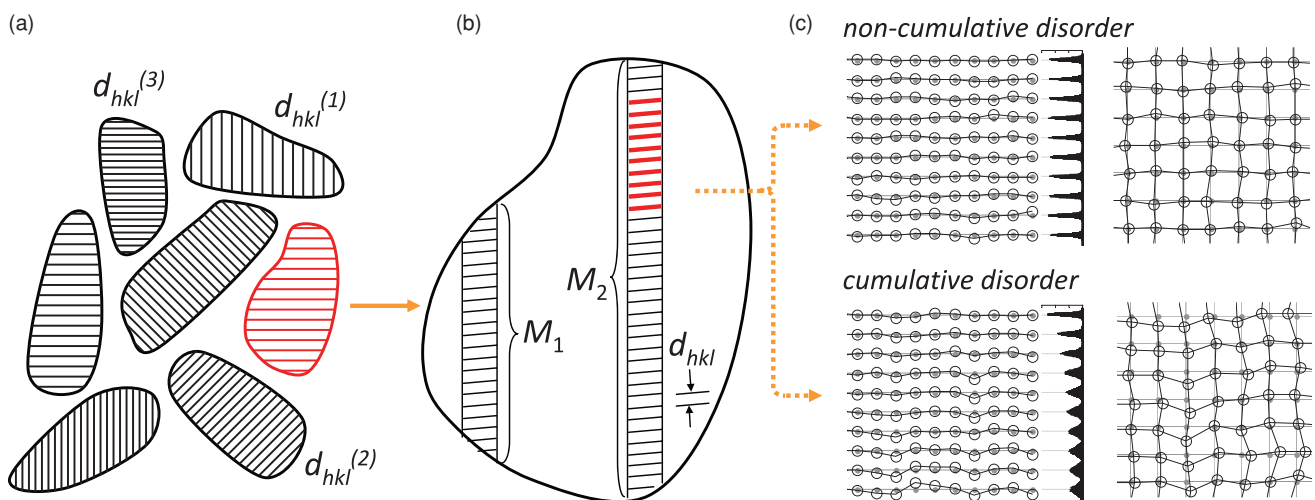

FIG. 1. (Color online) Different mechanisms responsible for diffraction peak broadening. A collection of crystallites of different shapes and sizes is sketched in (a), showing a slight variation of the interplanar distance d_{hkl} from one crystallite to another (lattice-parameter fluctuation). The column length M in a crystallite can depend on its shape as shown in (b). Noncumulative vs cumulative disorder is sketched for a small number of diffracting planes in (c). Noncumulative disorder (top) involves random fluctuations about the ideal lattice positions (gray); for cumulative disorder (bottom), statistical fluctuations about the lattice spacing occur, which accumulate to destroy the ideal lattice. The histograms shown are the lattice positions of 10 000 one-dimensional (1D) simulated lattices, showing the loss of predictive ability due to distortion propagation that is the signature of paracrystalline disorder. Sketches of disordered two-dimensional (2D) lattices are shown in the far right, with the ideal lattice indicated by dotted gray lines.

functional dependence $\Delta_q(m)$ when only a limited number of higher-order reflections are observable. This is especially true for highly defective organic materials, where only a few (typically two or three) higher-order peaks can be observed.

More accurate techniques involve utilizing the entire peak shape, in the form of a Fourier-transform (FT) analysis of the diffraction peaks. The power of such techniques, first introduced by Warren and Averbach,[16,17] is that contributions from cumulative disorder and a finite crystallite size can be decoupled due to their specific functional dependences on diffraction peak order and the Fourier frequency. The Fourier coefficients of the peaks can be represented as the product of contributions from a finite crystallite size, which is independent of peak order, and disorder terms that are peak-order dependent.[8,18] This Warren-Averbach (WA) analysis has utility on multiple length scales and for different materials systems, not only the organic systems described herein. A useful comparison of Scherrer, integral breadth, and Fourier-based (WA) techniques has been provided for ball-milled molybdenum by Lucks *et al.*[19] While the WA analysis has been successfully applied to defective metals,[20–23] ceramics,[24–26] composites,[27] and to a lesser extent, polymers,[8,18,28,29] it can be easily applied to systems with much larger average layer spacings provided diffraction data can be collected and the diffracted line shapes are well resolved and sufficiently above background. Such systems include biological moieties (i.e., lipids or proteins), block copolymer domains, and colloidal crystals. For example, in colloidal crystals, the quantification of disorder and domain size can be of great importance in the study of optical trap states for photonic applications[30] which could be determined by analogy with ultraviolet diffraction spectra analysis.[31,32]

In this work we focus on organic semiconducting thin films, where the highest performing materials are often highly textured, semi- or polycrystalline films. Organic semiconductors have been thoroughly studied—and in some cases commercialized—as active layer materials in complementary logic circuits, photovoltaics, lighting, and sensors. They are readily solution processed and are thus amenable to low-cost, high-throughput fabrication.[33–35] The ability to design new molecules and predict their performance in devices suffers from a lack of well-understood structure-property relations. In part, this is due to the drastic variability in microstructure and morphology caused by variations in chemistry, processing conditions and postprocessing treatments which in turn affect device performance.[36] One aspect that makes organic thin films particularly susceptible to disorder is the presence of weak van der Waals interactions between molecules. Electronic coupling is strongly dependent on details of intermolecular separation. The nature of frontier orbital overlap in π-conjugated materials is found to be highly sensitive to small variations in intermolecular spacing, orientation, and relative position.[3,37] The need to understand microstructure and morphology on multiple length scales thus motivates accurate determination of crystallite size and cumulative disorder. Such findings will aid in bridging the effect of chemistry and processing conditions with overall performance in optoelectronic devices such as organic transistors and photovoltaics.

Some disorder in organic semiconductor crystallites results from thermal (noncumulative) fluctuations (a description that is at the core of dynamic disorder models of charge transport).[38–40] Intrinsic static structural imperfections such as chain ends, twists in polymer backbones, as well as extrinsic defects such as stacking faults, impurities, or solvent swelling can also contribute to the cumulative lattice disorder most likely affecting the lattice parameter fluctuation, e_{rms}, and paracrystalline disorder, g. While peak-shape analysis cannot be used to determine the direct causes and mechanisms that contribute to the static disorder within the film, it does serve as a tool to thoroughly quantify disorder and therefore can contribute to the modeling of structure and charge transport in realistic films.[4,38]

While a number of x-ray-based techniques have been previously used to determine crystallite size and have addressed disorder, these techniques are prone to misuse or lack clear confidence bounds. Furthermore, the application of these techniques to organic semiconductors has been limited,[18,41,42] which is surprising given the importance of intracrystalline lattice disorder on charge transport. In this work we utilize a similar formalism as that of the WA analysis,[5,8,11,18] but we employ a direct fit to the experimentally determined Fourier coefficients of the peak shapes. We incorporate careful background subtraction and error propagation to provide not only more accurate final results for crystallite size, lattice parameter fluctuation, and paracrystallinity, but importantly, confidence in those results. We choose three organic semiconductors with distinct microstructures to highlight a range of crystallite sizes, disorder, scattering geometries, and crystallographic directions which are all accessible to WA analysis.

We first use the polymer poly{[*N,N* 9-bis(2-octyldodecyl)-naphthalene- 1, 4, 5, 8-bis(dicarboximide)-2, 6-diyl]-*alt*-5,59-(2,29-bithiophene)}, P(NDI2OD-T2), and show step by step how the full routine is performed. P(NDI2OD-T2) is an electron-transporting polymer that has been shown to have high, 0.1–0.8 cm^2/V s, mobilities in the top gate geometry. It is highly soluble and shows exceptional stability in ambient.[43,44] The small molecule triisopropylsilyl pentacene (TIPS-pentacene) is next used to show a small molecule system known to crystallize extensively as a comparison with the previously described polymer. TIPS-pentacene, also solution processable, consistently attains mobilities in the range of 0.1–1 cm^2/V s, but has been shown to exhibit bandlike transport and mobilities up to 5 cm^2/V s.[45–47] Finally, we show the case of an aligned film of poly(2,5-bis(3-alkylthiophen-2-yl)thieno[3,2-*b*]thiophene) (PBTTT) to explore the disorder associated with crystallographic directions directly linked to charge transport in conjugated polymers. PBTTT is a high mobility (up to 1 cm^2/V s), solution-processable polymer that has been well studied and shows significant order for a semiconducting polymer thin film.[48–50]

In addition to reliable results and successful application of the WA model to organic films, we show that the determination of crystallite size using diffraction techniques becomes irrelevant in systems where cumulative disorder dominates and arrive at a closed form for approximating a coherence length using the disorder terms described herein. Finally, we discuss the relation between the functionality of peak shape (in the form of pseudo-Voigt functions) and the WA parameters, highlighting the potential for a more accessible approach to

generally determine disorder contributions without involved FT methods.

II. THEORETICAL BACKGROUND

Before addressing the particular implementation of the Warren-Averbach formalism used in this analysis, it is helpful to describe the general aspects of the theory. This will help define the relevant variables and the ways they are included in the analysis.

Consider an arrangement of planes of atoms or molecules along a given crystallographic direction (hkl) and label the x-ray-diffraction peaks as $m(hkl)$, where $m = 1, 2, 3, \ldots$ is the diffraction order and d_{hkl} is the interplanar separation. We turn our attention to a unit cell on the jth plane from the origin of the crystal along the (hkl) direction. If the lattice was perfect, the distance from the origin, along the (hkl) direction, would be $|\boldsymbol{r}_j|_{hkl} = j d_{hkl}$. Allowing for disorder and imperfections in the lattice, we introduce terms involving fluctuations in the interplanar spacing (δd_{hkl}) and in the position of the planes with respect to each other (δj). This allows us to write

$$(\vec{r_j})_{hkl} = (d_{hkl} + \delta d_{hkl})(j + \delta j)$$
$$= d_{hkl} j + d_{hkl} \delta j + j \delta d_{hkl} + \delta j \delta d_{hkl}. \quad (3)$$

Keeping only first-order terms and renaming the deviations to correspond to the usual notation of positional disorder $Z(j) = \delta j$ and lattice parameter fluctuations $e = \delta d_{hkl}/d_{hkl}$, the interplanar separation is

$$(\vec{r_j})_{hkl} = d_{hkl}[j + Z(j) + je]. \quad (4)$$

The scattering amplitude for a scattering vector $\boldsymbol{q}$ is the sum of the waves coming from all the scatterers, and the intensity is the product with its complex conjugate

$$I(q) \propto \left[\sum_j \exp(i\,\vec{q}\cdot\vec{r_j}) \right] \cdot \left[\sum_{j'} \exp(-i\,\vec{q}\cdot\vec{r_{j'}}) \right]$$
$$= \sum_{j,j'} \exp[i\,\vec{q}\cdot(\vec{r_j} - \vec{r_{j'}})]. \quad (5)$$

Here, for simplicity, we ignore the structure factor associated with the (hkl) reflection since it does not influence the peak shape. The measured intensity will be the ensemble average

$$I(q) \propto \left\langle \sum_n N(n) \exp[i\vec{q}\cdot(\vec{r_n})_{hkl}] \right\rangle$$
$$= \sum_n \langle N(n) \exp[iqd_{hkl}(Z_n + ne)]\rangle \exp[id_{hkl}nq]$$
$$= \sum_n A_m(n,q) \exp[id_{hkl}nq], \quad (6)$$

where $(\boldsymbol{r}_n)_{hkl} = (\boldsymbol{r}_j - \boldsymbol{r}_{j'})_{hkl}$, $Z_n = Z(j) - Z(j')$, and we have grouped all sets of unit cells in the sample that are $n \geqslant 0$ repeat planes apart along the same column into a multiplicity factor $N(n)$. Finally, we can regroup terms as $A_m(n,q) = \langle N(n) \exp[iqd_{hkl}(Z_n + ne)] \rangle$. This last expression resembles a Fourier transform except that the Fourier coefficients are q dependent. For a peak centered at q_o, $q = q_o + dq$, and dq multiplies the fluctuations dependent on Z_n and e, which are small; so to first order, the approximation $A_m(n,q) \approx$

$A_m(n,q_o)$ is valid. Since n is a separation distance, $n \geqslant 0$, we can expand the complex exponential into a sine and cosine component and keep only the even part of the sum, the cosine series. Noting that for the mth-order diffraction peak, Bragg's condition is $d_{hkl}q_o = 2\pi m$ and that $N(n)$, Z_n, and e are independent variables, one obtains $A_m(n) \approx \langle N(n) \rangle \langle \exp(i2\pi m Z_n) \rangle \langle \exp(i2\pi mne) \rangle$, which is the usual separation of the Fourier coefficients into a size-dependent term and disorder-dependent terms. Now we turn our attention to each of these terms.

For the calculation of $\langle N(n) \rangle$ we need to determine the number of pairs of planes $\{j_1, j_2\}$ with $|j_1 - j_2| = n$ within a column consisting of x total planes. Since order is not important, choosing the pair $\{j_1, j_2\}$ is equivalent to the pair $\{j_2, j_1\}$ and we can show that there are $N(n,x) = x - n$ pairs in the column. Considering a normalized probability distribution $\rho_N(x)$ of column lengths within the sample, the sample-averaged size coefficient, normalized by the average column length M, is

$$A_m^S(n) = \frac{\langle N(n) \rangle}{M} = \frac{\int_n^\infty \rho_N(x)(x-n)dx}{\int_n^\infty \rho_N(x)x\,dx}, \quad (7)$$

where the lower integration limit in the numerator means that only columns of size $x \geqslant n$ can have a pair of planes n repeat units apart. The normalization by the average column length is to ensure that $A_m(0) = 1$.

As for the disorder terms, it is generally assumed that Z_n and e follow Gaussian statistics, and so the statistics of normally distributed random variables can be used. Since the mean value for the disorder variations is zero, $\langle Z_n \rangle = 0$ and $\langle e \rangle = 0$, we obtain $\langle \exp(i2\pi m Z_n) \rangle = \exp(-2\pi^2 m^2 \langle Z_n^2 \rangle)$ and $\langle \exp(i2\pi mne) \rangle = \exp(-2\pi^2 m^2 n^2 e_{\mathrm{rms}}^2)$, where we define the root mean square of the lattice variations in the sample, $e_{\mathrm{rms}} = \sqrt{\langle e^2 \rangle}$.

Finally, the positional disorder term Z_n is considered. For noncumulative disorder, the positional variation is about the perfect lattice and the relevant disorder is that for the pair $\{j_2, j_1\}$ of diffracting planes. These are independent; so $\langle (Z_n)^2 \rangle = 2\langle (Z_0)^2 \rangle$ and

$$\langle \exp(i2\pi m Z_n) \rangle = \exp\left(-4\pi^2 m^2 \langle Z_0^2 \rangle\right). \quad (8)$$

There is no dependence on n—the only effect is to reduce the peak intensity, as mentioned previously. For cumulative disorder, the positional variations are independent but they add so that $\langle (Z_n)^2 \rangle = ng^2$, with the paracrystallinity $g = \sqrt{\langle Z_0^2 \rangle}$, and

$$\langle \exp(i2\pi m Z_n) \rangle = \exp(-2\pi^2 m^2 ng^2). \quad (9)$$

Thus, we arrive at the well-known Warren-Averbach expression for the Fourier coefficients factored into the size- and disorder-dependent terms, $A_m^S(n)$ and $A_m^D(n)$, respectively.

$$A_m(n) = A_m^S(n)A_m^D(n)$$
$$= \frac{\langle N(n) \rangle}{M} \exp\left[-2\pi^2 m^2 \left(ng^2 + n^2 e_{\mathrm{rms}}^2\right)\right]. \quad (10)$$

For the size-dependent term, we consider two cases. In the case where all the crystallites are assumed to be of the same size, their distribution is described by a delta-function distribution at the column size $M = M_\delta$. To allow the more physically reasonable case where the column lengths of crystallites are not all the same, we describe the population of column sizes using a gamma distribution with a mean column length $M = M_\gamma$ and standard deviation w_γ.

III. EXPERIMENTAL

A. Materials

Poly{[N,N 9-bis(2-octyldodecyl)-naphthalene-1,4,5,8-bis (dicarboximide)-2, 6-diyl]-*alt*-5, 59-(2, 29-bithiophene) } [P(NDI2OD-T2), Polyera ActivInk N2200] was obtained from Polyera Corporation, Skokie, IL. TIPS-pentacene was obtained from Merck Chemicals. Solutions of 1 wt% (∼10 mg/mL) TIPS-pentacene and 1 wt% P(NDI2OD-T2) were prepared in 1,2-dichlorobenzene and were filtered in a 20 μm polytetrafluoroethylene filter. PBTTT was used as received and dissolved at a concentration 15 mg/mL in a solvent mixture of 6:1 chloroform/1,2-dichlorobenzene at 70 °C in a valve-sealed, pressure-resistant vial.[51]

B. Film fabrication

Substrates for all x-ray experiments were Si(100) wafers with native SiO$_2$ and were cleaned by sonication in acetone and isopropyl alcohol before a 20 min UV-ozone treatment. Films of P(NDI2OD-T2) were prepared on octadecyltrichlorosilane (OTS) -treated substrates. OTS was applied to cleaned substrates in hexadecane solution (0.1% by volume), for 10 min before rinsing with heptane, acetone, and isopropanol. P(NDI2OD-T2) was spun from an 80 °C, 1 wt% solution at a spin speed of 1200 rpm, and then annealed at ∼300 °C for 40 min in a N$_2$ glovebox, resulting in film thicknesses of ∼60–70 nm as measured by atomic force microscopy. TIPS-pentacene was spun from an 80 °C, 1 wt% solution at 1000 rpm, resulting in film thicknesses of 100–110 nm. PBTTT was deposited via a previously described flow-coating technique.[51] The substrate was adhered to a custom-built, motorized translation stage. Approximately 15 μL of the PBTTT solution was dispensed into the gap under the stationary knife blade fixed at 150 μm above the substrate surface. The stage was then translated at 2 mm/s in the direction of blade tilt. Once the films were dry, they were removed from the stage and heated to 250 °C for 5 min before cooling to room temperature. Film thicknesses were ∼30 nm. The aligned PBTTT films are misoriented ∼15° from the primary crystallographic axes of the Si wafer to avoid contributions from the Si substrate scattering peaks.

C. X-ray scattering measurements

X-ray-diffraction measurements on all samples were conducted at the Stanford Synchrotron Radiation Lightsource at beam lines 2-1 (high-resolution specular diffraction), and 7-2 (high-resolution grazing incidence diffraction). The data are expressed as a function of scattering vector $\boldsymbol{q}$, which is decomposed into the components parallel to ($\boldsymbol{q}_{xy}$) or normal to ($\boldsymbol{q}_z$), the substrate depending on the desired scattering geometry. The incident photon energy was 8 keV for both beam lines. All diffraction experiments were carried out with the samples enclosed in a helium-filled chamber in order to reduce the effects of air scattering and beam damage due to the intense x-ray beam. While the primary effect of beam damage is to reduce peak intensity with no change in peak position, the uniform sample was periodically translated during a single scan because peak shape is of central importance to the analysis described herein. For thin polymer samples, beam damage can become noticeable during a long, single scan and can introduce artificial broadening in the higher-order peaks. In cases with very low scattered intensity, the sample was translated after each recorded diffraction peak. A good way to check for beam damage is to compare fast scans (with necessarily poorer counting statistics) to the final data, normalized to match intensities. The faster scans should each be taken at fresh spots in the sample, with varying integration times and point densities.

For the grazing incidence x-ray scattering (GIXS), the films were illuminated at incidence angles of about 0.2° (7-2 measurements). These values were chosen so that the x-ray beam penetrates the entire thickness of the polymer sample (∼50–100 nm) but only a small portion of the silicon substrate.[52,53] This choice reduces the background scattering from the substrate.

Beam footprint and Lorentz corrections must be applied to the measured diffracted intensity.[48] The beam footprint correction takes into account that changing the scattering angle 2θ also changes the volume of the sample that is illuminated by a factor of $\sin\theta$. The Lorentz correction accounts for the different amount of time that a given reciprocal lattice point spends at Bragg condition, which varies as $\sim\sin\theta$. The polarization correction is not taken into account due to the highly polarized nature of the used synchrotron radiation. Both these corrections put together require us to multiply the original data by a factor of q^2.

The q resolution of the data obtained at the beam lines used is determined by the collimation on the detector. For the high-resolution specular scattering (beam line 2-1), the collimation was set by fixed slits with a resolution of 0.01° or about 0.01 Å^{-1} for the scattering vector, $\boldsymbol{q}_z$. For the high-resolution grazing incidence scattering (beam line 7-2), the diffracted beam collimation was set by 1 mrad Soller slits (effectively 0.1° or a $\boldsymbol{q}_{xy}$ resolution of 0.007 Å^{-1}).

With Fourier-transform techniques, especially those requiring peak-fitting routines, it is important for the collected data to be of high quality throughout, not just at or near the peak centers. Significant information must be collected from the low-intensity peak wings, and thus, long integration times are often necessary especially for weakly diffracting samples. In general, having more points per peak is advantageous for the fitting procedure used to subtract background. Collecting a broad region around each peak is important for having a high point density in the Fourier-transformed data. Thus, more points and collected breadth around the diffraction peaks are important for error reduction and background subtraction. Nevertheless, a compromise must be made between collection time and analysis requirements. We have found that collecting data centered about a peak in a window of 6–10 times the full width at half maximum with ∼100 points in this range for each peak is sufficient.

TABLE I. Peak parameters for P(NDI2OD-T2) data set.

Index	Position, q_z (Ref. [56]) ($Å^{-1}$)	Area, A (arb. units)	Width, Δ_q ($Å^{-1}$)	Pseudo-Voigt mixing parameter, η
100	0.258	0.0368	$0.02033 \pm 7 \times 10^{-5}$	0.739 ± 0.007
200	0.510	0.0014	$0.0325 \pm 2 \times 10^{-4}$	0.72 ± 0.01
300	0.759	2.6×10^{-4}	$0.0469 \pm 8 \times 10^{-4}$	0.94 ± 0.03
400	1.017	1.5×10^{-4}	0.071 ± 0.002	0.72 ± 0.07
500	1.259	1.1×10^{-4}	0.104 ± 0.006	1.0 ± 0.1

IV. DATA PROCESSING AND ANALYSIS

A. P(NDI2OD-T2)

We will use the data set of a thiophene-naphthalene polymer with branched alkyl side chains, P(NDI2OD-T2), as an example to describe each step in the analysis process. The diffraction data [Fig. 2(a)] are from the out-of-plane lamellar stacking of the copolymer. While this polymer normally adopts a face-on molecular packing,[54] the edge-on packing can be achieved by annealing a spun cast film to the melting point and slowly cooling the sample to ambient temperature.[55] This stacking comprises the layered conjugated cores of the polymer (see the inset to Fig. 2), separated by the branched alkyl chains of the naphthalene-diimide, and has a large mean lattice spacing of $d_{100} = 24.4$ Å. The obtained size and order parameters describe, respectively, the size of the layered lamellae in the direction perpendicular to the substrate and the fluctuations and/or disorder associated with the molecular packing in this direction. We use this data set as a model since five well-resolved peak orders are observed. In the following sections, the same formalism is applied to other materials systems.

As a starting point, one measures the desired x-ray diffraction (XRD) pattern and determines the uncertainty in each of the data points (see Appendix A). To propagate errors through the data analysis, the standard procedure is to keep track of the variance after each operation. The next step of refinement is to take into account that even when the error in the initial data may be uncorrelated, the error after manipulating the data could be correlated, as would be the case with fitting, Fourier transforms, and interpolations. This means that we must not only keep track of the variance in our variables, but also their covariance; we will use the covariance matrix formalism described in Appendix A. For now, it suffices to know that at each step we must calculate the new covariance matrix and for this we need to know the derivative of each output with respect to each input for all the operations in the process. The input and output in a given step can either be a set of data points or fitting parameters depending on the operation (e.g., least-squares fitting, Fourier transform, etc.).

After estimating the error in our raw data and performing the initial q^2 correction, we determine the background to subtract from our data and isolate the diffraction peaks. An accurate determination of the functions describing the background and peaks is needed so that there is confidence in the isolated peaks in both high- and low-intensity ranges to avoid errors in the low-frequency components of the Fourier spectrum. This is done with a two-step fitting routine in which a coarse fit to the entire data set is done first, serving to determine the functions that span the entire data range—mainly the background

functions and (if present) broad amorphous scattering peaks. Following this initial fitting step, a refinement is performed by considering a reduced range of data around each of the diffraction peaks of interest. The fitting parameters allowed to vary in this refinement step are only those that most influence the fit within the reduced data range, for example, the parameters of the peak of interest, and the width of adjacent peaks (those parameters defining the wings of nearby peaks). This refinement step is repeated for each of the diffraction peaks.

In the case of P(NDI2OD-T2), the functions used to describe the data are two background functions (an exponential and a power-law function), collectively labeled f_{bkg}, and five pseudo-Voigt peaks, one to describe each peak order f_{pV}^m. The peak positions, widths, amplitudes, and pseudo-Voigt mixing parameters for each diffraction order are reported in Table I.

The intensity from each diffraction order is then isolated from that of the remaining peaks and background. It should be noted that the isolated peak, $F^{(m)}$, is not the same as the function describing the peak in question, f_{pV}^m. The function f_{pV}^m is used as a means to more accurately determine the functions describing the background and remaining peaks. The isolated peak is obtained as the difference between the original data, Y_{data}, and both the global background, as well as background intensity from nearby peaks:

$$F^{(m)}(q) = Y_{data}(q) - f_{bkg}(q) - \sum_{i \neq m} f_{pV}^{(i)}(q). \quad (11)$$

Note that the sum is over all peaks except that being isolated (peak m). This approach is used to minimize the effect of the background or surrounding peak wing subtraction errors, which can give rise to artifacts in the analysis. Furthermore, if an appropriate background determination is prevented due to noise in the data or a low peak intensity, the resulting error in the isolated peak will reflect this (it will be large). Such an effect can be observed in the higher-order peaks, especially the wings of $m = 3$, as well as peaks $m = 4$ and 5 [Fig. 2(b)].

The isolated and centered individual peaks are shown in Fig. 2(b)—normalized only for display purposes—showing order-dependent broadening indicative of the non-size-related terms contributing to the peak shape. After isolating the individual peaks, we calculate the coefficients of the Fourier series with a fast-Fourier-transform (FFT) algorithm [Fig. 2(c)]. Here, the validity of the assumption that the peaks are symmetric can be verified by plotting the inverse Fourier transform of the even and odd parts of the FFT, representing the cosine and sine series, respectively. As shown in Fig. 2(b), the cosine series describe the isolated peak shapes well, while
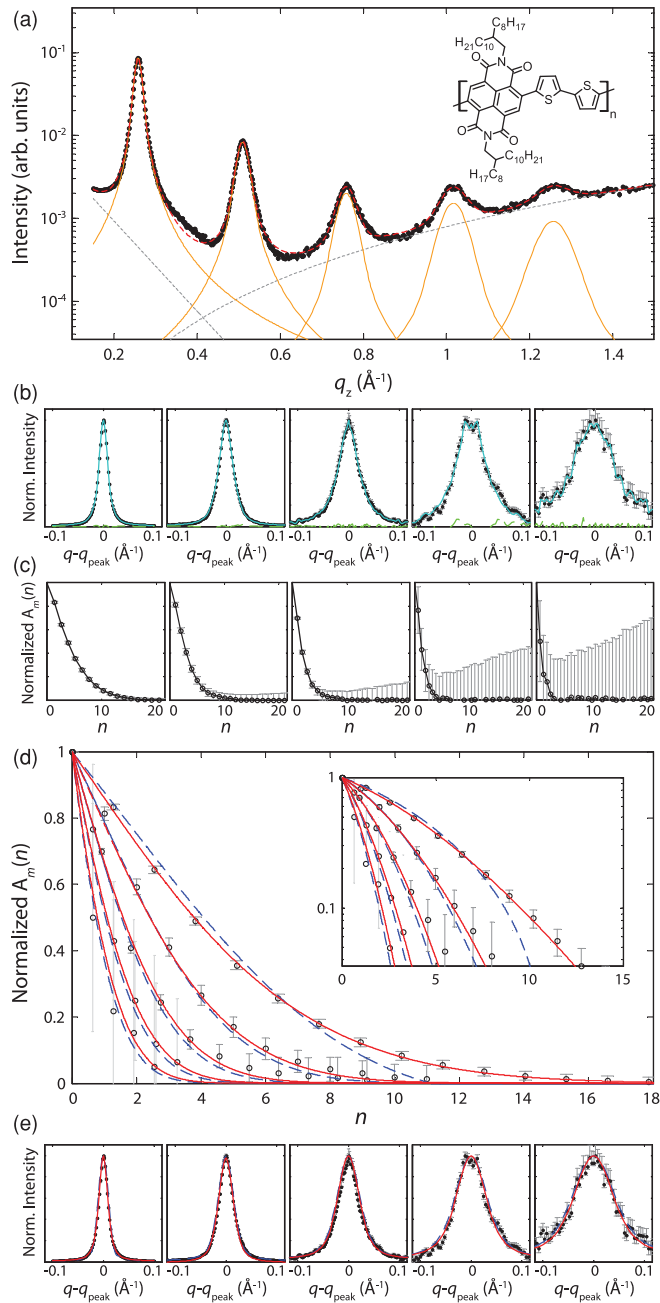
FIG. 2. (Color online) Data processing and weighted Warren-Averbach full-fit analysis of P(NDI2OD-T2) along the lamellar stacking, specular diffraction direction. (a) Corrected data with measurement error, on a semilogarithmic scale, with coarse fit functions for individual peaks (solid orange), background (dotted gray), and the combined coarse fit (dashed red); inset: chemical structure of P(NDI2ODT2). The isolated peaks for $m = 1$ to $m = 5$ (b) and their respective normalized Fourier transforms (c) with the associated propagated error. The peak contribution from the cosine (solid cyan) and sine (dashed green) terms are shown with the raw isolated peaks in (b). The large errors for higher diffraction order peaks [especially (400), (500)] are shown here to reflect the uncertainty associated with multiple processing steps with these poorly resolved peaks. The weighting used in FT fits is based on these error values, thus, the FT data points with excessive error (those with the least certainty) play little role in the final FT fit. (d) The normalized Fourier transforms with the weighted WA full fits assuming

the sine components only become noticeable when the noise in the data increases.

When these normalized Fourier spectra of the isolated peaks are fitted to the WA function, $A_m(n)$ [Eq. (10)], the contribution of each data point to the fits is weighed by its uncertainty. The resulting fits are shown in Fig. 2(d), where two different column-length distributions are assumed. In one case, it is assumed that all the columns in the sample have the same length (a delta-function distribution), and in the other, a gamma-distribution function is used. The comparison between these two approaches is described below, but the gamma distribution yields better fits to the data. This is due to a more realistic size distribution, as well as an extra fitting parameter. Finally, the ability of the Warren-Averbach formalism to describe the original shape of the isolated peaks is shown by calculating the inverse Fourier transform on the fitted WA function and comparing it to the isolated peaks [Fig. 2(e)]. Reassuringly, the gamma-distribution-based fit results provide the best agreement.

The fitting results are summarized in Table IV along with those for the other two materials analyzed here. The average P(NDI2OD-T2) column length is $M = 22$ nm (using the results that assume a γ distribution), with a paracrystallinity parameter of $g = 3.6\%$ and an interplanar spacing fluctuation of $e_{rms} = 1.7\%$. These parameters are consistent with those expected for a polymer system along a crystallographic direction where layers are separated by disordered alkyl side chains, leading to unregistered stacking of two-dimensional (2D) sheets.[18] These results are compared to those obtained with a number of peak breadth and shape analysis techniques in Table IV, and a more detailed discussion is provided in following sections. The results of the routine described herein agree reasonably well with other analysis techniques described earlier (Scherrer, integral breadth, and graphical WA methods), with the added benefit of using as much information as possible to determine the fitting parameters, using the error in the data to weigh the fits and provide a conservative estimate of uncertainties.

It should be noted, however, that the uncertainty in the results reflects the propagated error through the different steps in the analysis but it does not account for the (still existent) errors in background determination. To determine the effect of these errors, the analysis process was repeated on the same data set but using several different background subtractions. This had little effect on the column lengths, but the disorder terms (g, e_{rms}) varied within 0.5–1 %. As a separate validation, data sets from two different films prepared nominally the same way yielded results that were also within this range. This measure of analysis-to-analysis and sample-to-sample variation serves as an estimate of the systematic errors associated with this line-shape analysis.

B. TIPS-pentacene

Another prototypical material is the soluble acene small molecule TIPS-pentacene, due to its high mobility with the

---

a column-length distribution following a delta function (dashed blue) and a gamma function (solid red); inset: log scale representation of FT fits. (e) Resynthesis of the peaks in reciprocal space using the fit results shown in (d) match well with the raw data.
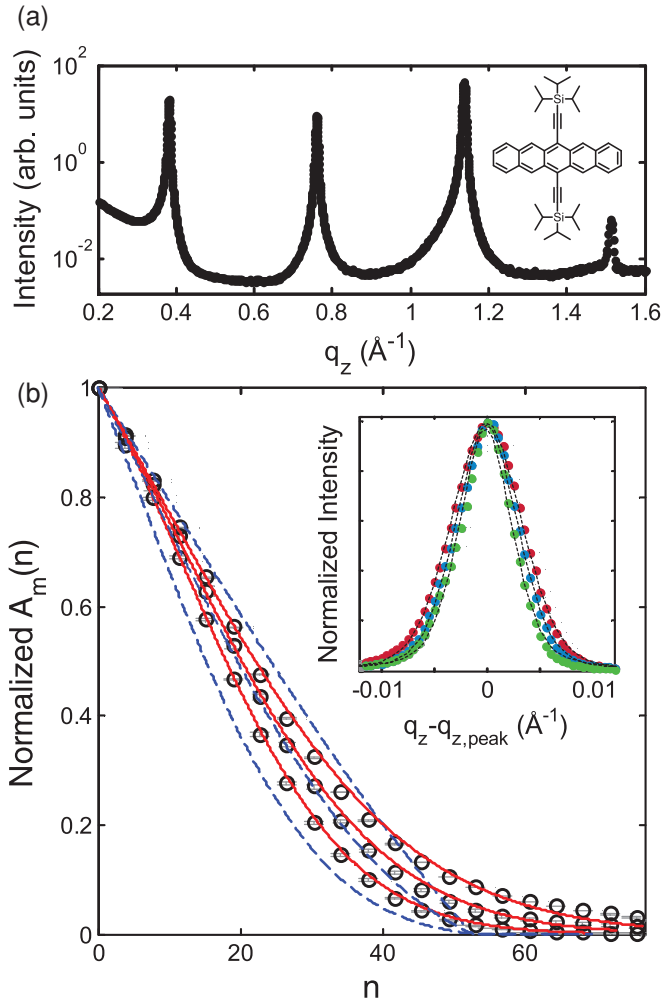
FIG. 3. (Color online) WA full-fit analysis of TIPS-pentacene specular diffraction. (a) Corrected specular data; inset: TIPS-Pn chemical structure. (b) Fourier transforms of the isolated peaks, with error, and fits utilizing delta (dashed blue) and gamma (solid red) distribution functions (inset: from narrowest to broadest, the 001, 002, 003 peaks).

recent observation of band transport which has been attributed to very high-quality crystalline regions.[47] The diffraction data presented here is the out-of-plane packing of the highly textured thin film. Four orders of the $(00l)$ peak are observed, with the intensity of the fourth order appearing very low due to the structure factor. The spacing associated with this direction is $d_{001} = 16.4$ Å, in good agreement with previous structural determination.[46,57] The same corrections and analysis steps described in the previous section were applied here (Fig. 3).

The diffraction peaks are found to be much narrower than in P(NDI2OD-T2) (see Table II) and exhibit less order-dependent broadening as is clear from the isolated peaks shown in Fig. 3(b), inset. Slight peak asymmetry, most apparent in the (003) peak plotted on a semilogarithmic scale, has negligible effect on the analysis.

The low-frequency components of a peak, represented in the first few $A_m(n)$ Fourier coefficients, are the most sensitive to inaccuracies in background subtraction and overlap from tails of adjacent peaks. This is usually reflected in an unphysical concavity of $A_m(n)$ around $n = 0$, termed the "hook effect."[5] It is unphysical because the second derivative of $A_m(n)$ cannot be negative since it is proportional to the column-length distribution [Eq. (7)] which must be positive. Such errors result in an overestimation of the average column length in order to fit the terms at low n, and consequently an overestimation of the disorder terms in order to fit the terms at large n. A standard method to correct for this is to fit a line to the first few $A_m(n)$ coefficients, and normalize the calculated $A_m(n)$ to the intercept of that line instead of to $A_m(0)$. The first two diffraction orders for this data set showed a slight hook effect, and this correction was employed.

As with the P(NDI2OD-T2) data set, it is evident that the gamma distribution for column lengths yields a better fit to the experimental $A_m(n)$ values. The obtained column lengths point toward large crystalline domains, with an average column length of $M = 67$ nm, small fluctuations in the interplanar spacing ($e_{rms} = 0.18\%$), and a small paracrystallinity ($g = 0.3\%$). This agrees with the general knowledge that TIPS-pentacene exhibits a well-defined three-dimensional packing, necessitating a low paracrystallinity.

C. PBTTT

Although the study of the column length and disorder associated with all the crystallographic directions of an organic crystal allows us to relate its microstructure to performance, it is of particular importance to analyze those directions directly associated with charge transport in organic semiconductors. Charge transport in thin-film transistors occurs in the plane of the film, thus, an in-plane scattering geometry is of key importance to study directions directly associated with charge transport in thin film transistors. As an example, we investigate an aligned film of a fused ring polythiophene, PBTTT. This high-performing polymer exhibits highly textured edge-on packing with the chain backbone and cofacial π-stacking direction lying in the plane of the film.[48,59] Disorder that influences the π-stacking will disrupt the π-orbital overlap, thus directly affecting charge transport. The difficulty associated

TABLE II. Peak parameters for TIPS-Pn data set.

Index	Position, q_z (Ref. 56) (Å^{-1})	Area, A (arb. units)	Width, Δ_q (Å^{-1})	Pseudo-Voigt mixing parameter, η
001	0.380	1.0270	$0.00594 \pm 5 \times 10^{-5}$	0.48 ± 0.03
002	0.759	0.1333	$0.00690 \pm 3 \times 10^{-5}$	0.34 ± 0.02
003	1.136	0.3499	$0.00790 \pm 3 \times 10^{-5}$	0.30 ± 0.02
004	1.511	3.3×10^{-4}	$0.0102 \pm 2 \times 10^{-4}$	0.35 ± 0.06

with most conjugated polymers is that the π-stacking peak is often weak, and rarely are two or more orders observed. The use of an aligned film serves the dual purpose of (1) decoupling the π-stacking peaks from other in-plane scattering (i.e., the chain backbone repeat units)[54,59] and (2) increasing the observed intensity by narrowing the solid angle where there is scattering due to the π-stacked planes (the chains are aligned within $\sim 30°$).

The π-stacking spacing in this sample is 3.69 Å. Two diffraction orders are readily observable with some misaligned contributions from the chain backbone. By performing scans in the orthogonal direction [see Fig. 4(a)], we are able to fix the positions of the chain backbone and mixed index peaks (unrelated to the π-stacking) and subtract their contribution with the background when isolating each peak. The isolated peaks [Fig. 4(b), inset] are significantly broader than those from the previous two materials, and a clear order dependence of the

broadening is observed (see Table III). The resulting Fourier transforms have a large associated error due to the higher noise in the data, the added uncertainty of the contribution from the chain backbone peaks, and the low relative intensity of the second-order peak. These complications highlight the importance of using all the information contained in the data (fitting all the Fourier coefficients), as well as keeping track of the error at each step of the line-shape analysis.

One notices that the functional dependence of the column-length distribution (single length compared to gamma distribution) plays no role in the fits, as can be seen in Fig. 4(b) where they overlap. In fact, there are interesting effects associated with the description of the column length in this analysis. Most importantly, we observe a large paracrystalline disorder, $g = 7.3\%$, and a small but nonzero fluctuation in the interplanar spacing, $e_{rms} = 0.9\%$. We propose that with such a high degree of lattice disorder, the determination of a mean crystallite size by x-ray techniques is not possible, and we further address this point in a following section.

V. DISCUSSION

In the following discussion we compare the results using the routine applied above with other x-ray peak-shape-analysis techniques in order to highlight the benefits associated with our methodology. We investigate this from the standpoint of accuracy, confidence, and robustness in the resulting parameters. The effect and validity of the two column-length distributions used is addressed. We then discuss the difficulty in determining crystallite size when the inherent lattice disorder is dominant. This is important since the extraction of a crystallite size from single peak width is often misused. To make the case that size determination of heavily disordered crystallites is unreliable, we derive a closed-form coherence length based on the disorder parameters alone. Finally, as the full WA routine requires in-depth data processing and analysis, we describe a simpler method to compare lattice disorder across systems by exploring the pseudo-Voigt mixing parameter. This mixing parameter contains more subtle information about peak shape than the width alone, and can thus be used as a first-order comparison when considering disorder.

A. Benefits of weighted full fit with error propagation

The benefits of the full WA routine outlined here are presented by detailing the advantages of careful error propagation for confidence, fit accuracy, and robustness; we further compare this to other analysis techniques and discuss the respective results. The important point is that our methodology provides better, more accurate values for the crystallite size and disorder parameters than those obtained from these other methods.

Fourier-transform peak-shape analyses suffer from a number of assumptions with respect to background subtraction and can be subject to errors due to their multistep nature. It is thus important and informative to incorporate a complete error propagation routine so that confidence bounds can be established for the parameters of interest. Uncertainty due to fitting and peak isolation of poorly resolved peaks, which are complicated by uncertain background and partial overlap from adjacent reflections, can hinder analysis. Additionally, the same uncertain subtraction of background and adjacent
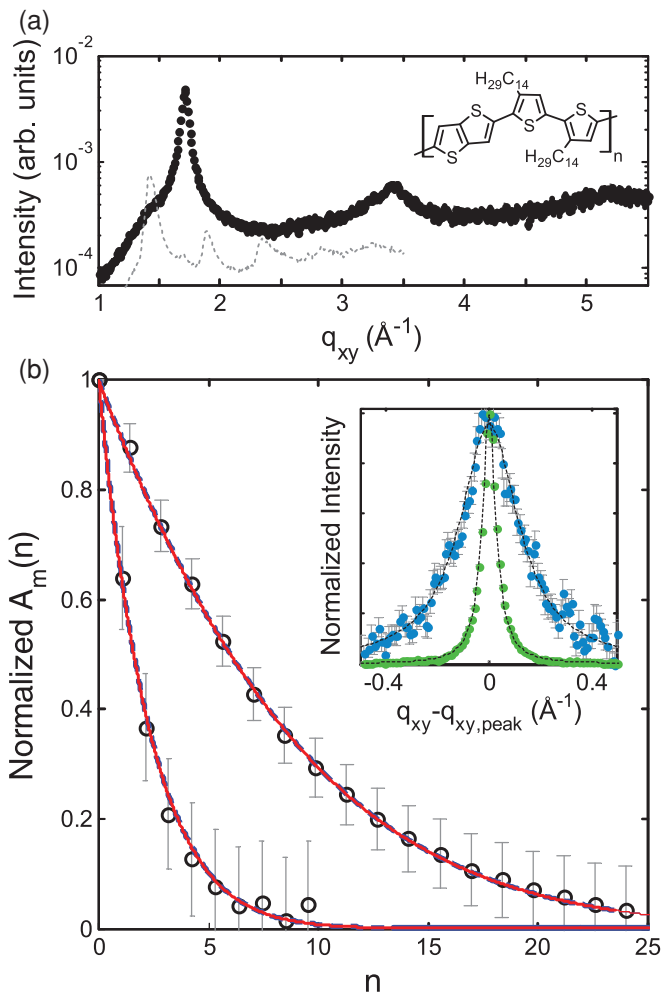
FIG. 4. (Color online) WA full-fit analysis of π-stacking grazing diffraction of PBTTT. (a) Corrected grazing incidence data with associated errors, as a reference, we include grazing incidence data in the orthogonal direction (dotted line) showing the peak positions of the chain backbone-related contributions; inset: PBTTT chemical structure. (b) FTs of isolated peaks, with error, and fits utilizing delta (dashed blue) and gamma (solid red) distribution functions (inset: from narrow to broad, the 010 and 020 peaks). Note that the fits to the FT data overlap regardless of the assumed size distribution.

TABLE III. Peak parameters for PBTTT data set.

Index	Position, q_z (Ref. [56]) (Å^{-1})	Area, A (arb. units)	Width, Δ_q (Å^{-1})	Pseudo-Voigt mixing parameter, η
010[a]	1.704	1.5×10^{-4}	$0.0652 \pm 5 \times 10^{-4}$	1.00 ± 0.01
020[a]	3.416	1×10^{-5}	0.28 ± 0.01	1.00 ± 0.07

[a]We have adopted the orthorhombic unit-cell indexing of Chabinyc *et al.* for PBTTT (Ref. [48]) although the unit cell is almost certainly triclinic (Ref. [60]). This is done for simplicity.

peak overlap reduces the confidence in the low Fourier frequency components and can give rise to the well-known hook effect. Taking into account the varying certainty in each Fourier component, one can obtain a more accurate fit to the model and a conservative estimate of confidence in the desired parameters. More refined statistical methods for error propagation can be performed, such as Monte Carlo bootstrap, but their application would narrow the error bounds for the obtained parameters and not modify the observed trends; their utilization is beyond the scope of this work.

Comparing our WA full-fit routine to similar diffraction analysis techniques is an informative way to understand advantages in our routine. Line-shape analysis techniques can be divided into those that use the q-space data, with the most prominent example being the Scherrer approach, and those that use its Fourier transform, such as the Warren-Averbach approach. In addition to the Scherrer analysis, another peak-breadth analysis is the method of integral breadths,[52,61] which is related to the Williamson-Hall analysis. In this routine, the size-related broadening of the peaks is not dependent on diffraction order, and order-dependent broadening, $\Delta_q(m)$, is assumed to vary linearly or quadratically with m. The crystallite size is obtained from Δ_q vs m fits.[11,12] For this method to be accurate, several diffraction orders are required, or the fits will not be reliable. In Fourier-transform techniques, the information contained in the complete peak shape is considered, not just the breadth.

The first application of the Warren-Averbach formalism, and the one most commonly used, relies on rewriting Eq. (10) as

$$\ln[A_m(n)] = \ln\left[\frac{N(n)}{M}\right] - 2\pi^2 m^2 n f(n), \qquad (12)$$

where $f(n) = g^2 + n e_{\text{rms}}^2$. Fitting $\ln[A_m(n)]$ vs m^2 for a constant n, one obtains values for $\ln[N(n)/M]$ from the intercept and $f(n)$ from the slope of each curve. Since multiple peak orders (m) are necessary for fitting, but the higher orders decay rapidly with n, the data becomes noisy and must be truncated, which leads to artifacts in the subsequent fitting steps. Fitting of $\ln[N(n)/M]$ vs n provides a value for M, and a third linear fit of $f(n)$ vs n yields g^2 and e_{rms}^2. One of the biggest disadvantages of this graphical implementation is that it is unreliable, since often the intercept and the slope of a linear fit are determined from as few as two or three points. This was addressed in the work of Prosa *et al.*[18] by employing a Monte Carlo bootstrap procedure to reflect the added uncertainties of using iterative fits. This is improved in our full-fit routine, since all the data are considered simultaneously when performing an error-weighted fit to the model.

The effect of a weighted fit of the $A_m(n)$ to Eq. (10) is further understood by considering the uncertainties of the experimental Fourier coefficients. For a constant m, the uncertainties in $A_m(n)$ for large n are due to noise in the data, while those for lower n suffer from error in the background and overlapping peak subtraction errors, for example when the hook effect is present in the data. In light of this, the points in the intermediate n region tend to be more heavily weighted. Additionally, the low-order $m(hkl)$ peaks are often the least noisy and most clearly resolved, since they are well above the noise floor and not overlapping with other diffraction peaks. Thus, the accuracy in the Fourier coefficients from these peaks is greater. This is clearly seen in the data [see Fig. 2(c)]. Thus, the benefit of complete error propagation is readily employed by performing a weighted least-squares fit.

A comparison of our full-fit WA method with the other analysis approaches highlights many of the inaccuracies or drawbacks inherent in these (Table IV). Results for Scherrer-derived coherence lengths are an overestimation both for TIPS-Pn and P(NDI2OD-T2). This is because this method yields a volume-weighted average size and makes assumptions regarding the shape of grains. This method of determination of crystalline coherence length assumes all broadening is due to size effects, which is not the case when the disorder-induced broadening is severe (e.g., PBTTT ribbon phase).

The results of the integral breadth approach, where the crystallite size is determined from the intercept of peak breadth vs. m^2 also overestimates size in P(NDI2OD-T2) and TIPS-pentacene for the same reasons as the Scherrer analysis. However, other inaccuracies arise in both the integral breadth and the graphical WA analysis implementation due to fitting with just a few points. Thus, linear trends are not always clear and there is a possibility that either the slope or intercept of the fitted equation is negative (e.g., size determination of PBTTT with graphical WA and integral breadth). This yields unphysical results, which we denote in Table IV, but does not suggest what to do in order to understand this issue. When using the full-fit version of the WA analysis, including error propagation, one can understand the physical mechanism responsible for the observed results of the graphical analyses. For example, in the next section, we will discuss the unreasonably large values and errors that are obtained for PBTTT size-related terms using our analysis and how it relates to disorder.

Another benefit of the analysis described here is the robustness of the results, shown specifically in the P(NDI2OD-T2) data set. By varying the number of peaks used in the analysis (from $m = 1, \ldots, X$, where X is a higher-order peak), we show that it only takes the inclusion of approximately two peaks to obtain reasonably close values of M, g, and e_{rms} to those obtained when all the peaks are used (see Fig. 5). In fact, we

TABLE IV. Results of peak-shape analyses.

Sample/data set, analysis method	d_{hkl} (nm)	M or L_c (nm)	w (nm)	g (%)	e_{rms} (%)
P(NDI2OD-T2) specular, $h00$	2.438				
Scherrer, L_c[a]		27.8			
Integral breadth, $\Delta_q(m^2)$; M_v		34.0			
WA graphical		23.5		4.6	1.1
WA full fit with error (δ distribution)		27 ± 1	0	3.8 ± 0.2	1.9 ± 0.2
WA full fit with error (γ distribution)		22 ± 2	14 ± 3	3.6 ± 0.2	1.7 ± 0.3
TIPS-Pn, specular, $00l$[b]	1.652				
Scherrer, L_c[a]		95.2			
Integral breadth, $\Delta_q(m^2)$; M_v		97.5			
WA graphical		73.6		–	0.26
WA full fit with error (δ distribution)		87 ± 1	0	0.84 ± 0.09	0.20 ± 0.02
WA full fit with error (γ distribution)		67 ± 2	36 ± 1	0.3 ± 0.1	0.18 ± 0.01
PBTTT grazing, $0k0/\pi$-stacking	0.369				
Scherrer, L_c[a]		9.0			
Integral breadth, $\Delta_q(m^2)$; M_v		–			
WA graphical		–		7.7	1.1
WA full fit with error (δ distribution)		n/a	0	7.3 ± 2.5	0.9 ± 0.6
WA full fit with error (γ distribution)		n/a	n/a	7.3 ± 2.4	0.9 ± 0.6
WA full fit with error (neglecting size)[c]				7.3 ± 0.7	0.9 ± 0.6

[a]Use of hook correction.

[b]Scherrer analysis with $K = 0.9$, M_v is a volume-weighted crystallite size.

[c]$A_m^S(n) = 1$.

n/a: means result and/or error is prohibitively large, and – means result cannot be determined or is unphysical.

show that using just the first-order peak with one or two of the lowest Fourier frequencies from the second-order peak results in values that are in good agreement with the fits to all peaks. This is especially useful in the study of weakly bonded organics and polymers where observation of multiple diffraction orders is experimentally difficult. Thus, while it is a definite advantage to have as many peak orders as possible, a reasonable approximation can often be obtained from a limited data set.

It is useful to consider the results of the routine when the fitting steps do not use a weighted least-squares technique, but instead use an unweighted version of the fitting method. This is shown in Fig. 5. The results for M, g, and e_{rms} converge to values that are similar to the weighted-fits technique, but show more fluctuations with larger swings around the convergence value and have larger error bars. Faster convergence as a function of the amount of data necessary for the analysis and smaller confidence bounds are two of the key advantages of using a weighted fitting routine.

B. Effect of column length distribution

For the application of peak-shape analyses, assumptions must be made about the functional form that describes the column-length distribution within the sample. These assumptions will not only affect the size-related terms, but also those associated with disorder (g, e_{rms}). Below we describe the merits of a size distribution where we assume either one column length (delta function) or a gamma distribution.

The experimental determination of a column-length distribution with the WA method has been shown in a number
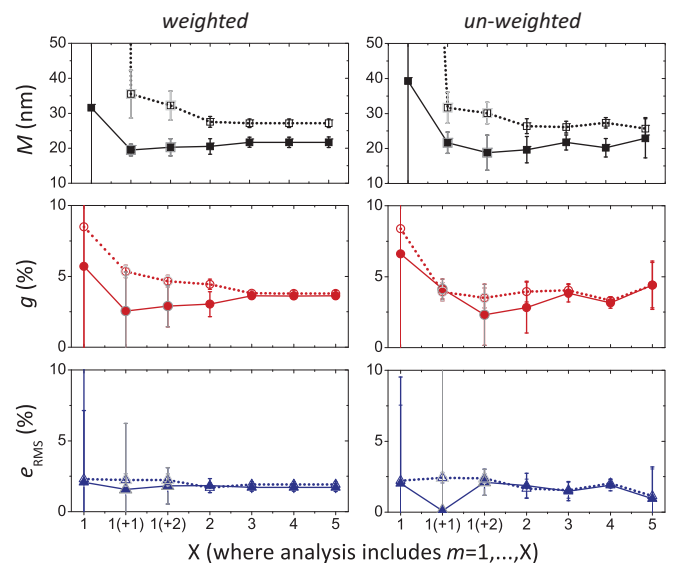

FIG. 5. (Color online) Robustness of full-fit analysis approach on P(NDI2OD-T2) data set. The fit results for M, g, and e_{rms} are shown for fitting routines incorporating weighted fits and compared to those without weights. Fits utilizing the γ size distribution are shown as solid lines and filled markers, while δ distributions are shown with dashed lines and open markers. X represents a fit incorporating peaks of order 1 through order X. The symbols at $X = 1(+1)$ and $1(+2)$ are fits for just the first peak ($m = 1$), with one or two of the lowest frequency orders from the second peak, which can give solutions nearing that of the full-fit five-peak analysis.
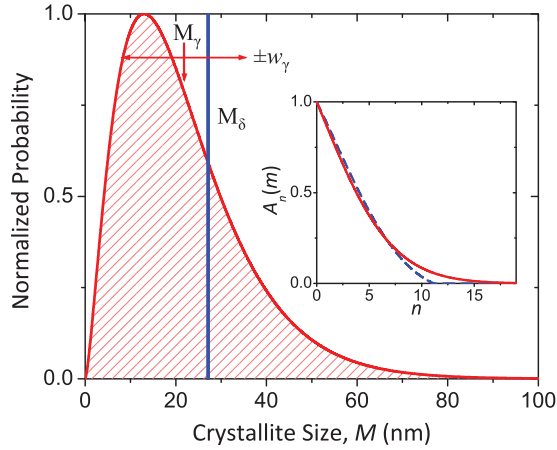
FIG. 6. (Color online) Size distributions determined from fit results of P(NDI2OD-T2) data set. The gamma distribution function (shaded red area) provides an average column length (M_γ) and variance ($\pm w_\gamma$) indicated by the arrows, while the delta function defines a column length of M_δ (blue vertical line). The relevant Fourier transforms of the (100) peak are shown as an inset, assuming each of these distributions (solid red for gamma function distribution, dashed blue for delta function distribution).

of cases,[62,63] particularly in materials where the contributions from disorder are not significant. This is due to the fact that the distributions are obtained from the second derivative with respect to n of the size-dependent term, $A_m^S(n)$ [Eq. (7)]. In the case of a small disorder contribution, one can approximate $A_m^S(n) \approx A_m(n)$ for small n in the first-order peak. The presence of disorder terms will limit the validity of this approximation. Also, calculating a second derivative numerically on quantities with a significant uncertainty (e.g., the Fourier components) will lead to a large error in the calculated crystallite size distribution.

Another option is to make an assumption about the functional form describing the distribution of column lengths[13,64,65] and parametrize the Fourier coefficients to the variables describing this distribution, thus obtaining an expression for $A_m(n)$ that can then be used in the least-squares fitting. A simple approach would be to describe the sample as a collection of columns with the same length, M_δ. While this is clearly not the case in real systems, it has the advantage of involving only one fitting parameter. The column-length distribution is often found to be markedly asymmetric with a broad tail extending toward larger sizes. Such a functional form is often modeled with a log-normal distribution. In this work we use a gamma distribution which is functionally similar to a log-normal[65] distribution and easier to implement. We show in Fig. 6 the extracted column-length distributions from the P(NDI2OD-T2) data set.

As can be seen in all the data sets presented here, the experimental $A_m(n)$ do not go abruptly to zero as necessary for a delta-function column-length distribution, but instead have significant curvature even in the absence of disorder terms. This is most noticeable in the Fourier transform of the first-order diffraction peak, as this peak is most affected by the contributions from the size distribution (Fig. 6, inset). One result of the inability of the delta-function distribution to describe the $A_m(n)$ is that this causes an overestimation

of M_δ, which is compensated by a slight overestimation of g and e_{rms}. Fits with the gamma distribution, then, describe the experimental $A_m(n)$ more accurately and yield better results when disorder does not dominate, as is the case for the P(NDI2OD-T2) and TIPS-pentacene data [Figs. 2(d) and 3]. The additional fitting variable associated with using a two-parameter gamma distribution rather than a one-parameter delta function is evident in the larger uncertainty in all the fitted parameters (Table IV). However, we argue that the benefit of a more physically reasonable distribution which yields better fits to the experimental Fourier coefficients far outweighs the slight increase in uncertainty. Last, in all three data sets, we note that the results for the distortion parameters (g, e_{rms}) are relatively insensitive to the assumed column-length distribution to within 0.5–1 % variation (similar to the variation observed from sample to sample or when assuming different background functionalities in one data set).

C. Effect of strong disorder on crystallite size determination with x-ray diffraction

When the lattice disorder within a crystalline grain becomes large enough, the connection between x-ray coherence length, as determined from the Scherrer expression [Eq. (1)], and crystallite size is lost. While at first this may seem like a trivial outcome, in the literature crystallite sizes are routinely quoted for strongly disordered systems based on peak breadth alone, and this point is often ignored in subsequent discussion. Moreover, there are a variety of concepts describing different characteristic crystalline length scales: crystallite size, grain size, column length, and coherence length. These are frequently used interchangeably in the literature, but this is not necessarily correct. For example, the connection between column length and crystallite size includes the use of an (often assumed) crystallite shape. In this section, we examine the relation between x-ray coherence length and column length for the case of strongly disordered materials.

Before doing so, however, it is instructive to critically examine the results from the PBTTT-aligned ribbon phase. At first it should be noted that any crystallite size-related term extracted from the fits suffers from error which renders this size meaningless. This is not due to the errors in the experimental $A_m(n)$, because the uncertainty in the disorder parameters is reasonable. It is also important to note that the values for g, e_{rms}, and the resulting $A_m(n)$ are not dependent on the functional form of the column-length distribution [see Fig. 4(b) and Table IV]. Unlike the other two data sets, where the delta and gamma distribution functions yielded noticeably different $A_m(n)$, especially in the first-order peak, this was not the case with the PBTTT data set. Even if we neglect size effects and set all $A_m^S(n) = 1$, the disorder terms are nearly the same as for the full fit with size terms (Table IV). These findings lead us to conclude that this diffraction data shows such a high degree of lattice disorder that the specifics of crystallite size have little effect on the peak shape (even on the first-order peak) and hence are undeterminable.

X-ray diffraction probes domains which scatter radiation coherently, and is dependent on the periodicity of the structure. Any disruption to the periodicity will reduce this coherence length. These disruptions can be localized (e.g., abrupt grain

boundaries) or continuous (i.e., cumulative disorder). In the context of disorder and its effect on coherence length, it is helpful to think of an infinite paracrystal, in which there are no abrupt changes in the periodicity and the loss of coherence is due to cumulative disorder alone.

One can define a disorder-associated coherence length, ξ, by calculating the breadth of a peak described by an infinite-sized crystallite with the only broadening mechanisms being paracrystalline disorder (g) and lattice-parameter fluctuations (e_{rms}). We then use this breadth and the Scherrer expression to calculate an effective x-ray coherence length. A detailed derivation of this expression is given in Appendix B. It is instructional, however, to look at one of its limiting cases. In the absence of lattice spacing fluctuations, $e_{rms} = 0$, one obtains

$$\xi = \frac{d_{hkl}}{2\pi g^2}. \tag{13}$$

This disorder-associated coherence length is inversely proportional to the disorder-related term (g) as expected. This is particularly useful for polymeric systems, where the weak nature of the van der Waals bonds and many degrees of conformational freedom make them highly susceptible to paracrystalline disorder. It must be kept in mind that the expression for ξ was obtained for the case of an infinite paracrystal, which means that it is valid as long as the disorder terms dominate and $A_m(n)$ becomes negligibly small before nd_{hkl} approaches the column length (physical size) of the paracrystalline domain, M, or $\xi \ll M$. Thus, an accurate determination of crystallite size by x-ray techniques on disordered materials is only possible if $\xi \approx M$ or $\xi > M$.

If we calculate ξ for the materials presented in this study, using the disorder terms obtained from their respective WA analyses, we see that for P(NDI2OD-T2) and TIPS-Pn, $\xi > M$, agreeing with the ability of the method to determine an accurate average column length (Table V). For the aligned PBTTT sample, as pointed out earlier, ξ is significantly smaller than for the other two samples. In fact, the disorder-associated coherence length ξ for the PBTTT-aligned film is comparable to that calculated with the Scherrer expression from the peak breadth; this is expected, since disorder is the dominant mechanism for peak broadening.

PBTTT is one of the highest performing p-type polymeric semiconductors, and is believed to be one of the most crystalline organic semiconducting polymers. These experimentally justified claims often relate to the very high degree of lamellar order (in the alkyl stacking direction, [h00]) of the liquid-crystalline layers of the polymer. The extrapolation of this high degree of order to other crystallographic directions, however, is not necessarily warranted. The aligned ribbon

TABLE V. Comparing coherence length and crystallite size.

Materials	M (nm)	ξ [a] (nm)	Scherrer, L_c (nm)
P(NDI2OD-T2)	22	170	27.8
TIPS-pentacene	67	18×10^3	95.1
PBTTT	N/A	10.1	9.0

[a]ξ utilizes results from WA full-fit results (γ distribution—see Table IV), M is also from the γ distribution fits.

phase represents a macroscopic orienting of this highly crystalline polymer, and yet our results indicate a degree of lattice disorder that is closer to amorphous than highly crystalline behavior in the π-stacking direction—so much that the x-ray determination of a crystallite size is impossible. These conclusions agree with recent findings that PBTTT grains show smooth transitions from one orientation to another.[66] The understanding of lattice disorder in the π-stacking direction is thus critical in the understanding of trapping mechanisms for this class of materials, and may define fundamental limitations for transport in π-conjugated polymers.

In short, when the majority of the broadening in XRD peaks comes from finite crystallite size (weak disorder), the Scherrer expression is a good approximation for the crystallite size. For samples with mild disorder, the contributions of size and disorder effects to the peak breadth are comparable and one must use techniques that allow the decoupling of the two, such as the integral breadth methods or Fourier-based (Warren-Averbach) techniques. For the accurate determination of disorder terms, the latter is preferred. Lastly, in the case of strongly disordered samples, disorder effects dominate the peak broadening and techniques based on diffraction line-shape analysis are unreliable for the determination of crystallite sizes. Indeed, the concept of crystallite size in such materials is not really valid.

A further consequence of this finding is that for highly disordered systems (where the x-ray coherence length of the sample is determined solely by disorder) the peak width alone can be used to estimate paracrystalline disorder (if the effects from lattice-parameter fluctuation, e_{rms}, can be neglected). Combining Eqs. (1) and (13), we arrive at

$$g = \frac{1}{2\pi} \sqrt{\Delta_q d_{hkl}}. \tag{14}$$

D. Insight into lattice disorder from trends in the pseudo-Voigt mixing parameter

The nature of a WA-type analysis, especially with the implementation of error propagation, can be time consuming and thus of less interest for studies where the specifics of lattice disorder are not the main focus. To encourage the use of peak-shape analysis for the determination of lattice disorder on a less involved level, below we explore the effect of cumulative disorder on the pseudo-Voigt mixing parameter. When used in conjunction with peak breadth, a simple comparison of paracrystallinity across samples or materials is possible. The following discussion considers disorder caused by normally distributed random fluctuations, as described in Sec. II.

In moving toward this simpler approach, we recall that contributions from size, paracrystallinity, and lattice-spacing fluctuations to the diffraction peak shape correspond to different functional forms.[67] It is known that the Fourier transform of a Gaussian function is a Gaussian, and the Fourier transform of an exponentially decaying function is a Lorentzian (also called a Cauchy line shape). Thus, from Eq. (10), we notice that the lattice-parameter fluctuation contributes to a Gaussian shape and the paracrystalline term is Lorentzian, which are results of the assumption that the disorder is Gaussian random. The size dependence is reasonably described by a

Lorentzian (for a delta-function column-length distribution). The actual shape of the peak in q-space will be the convolution of these contributions, and thus best described by a Voigt profile. Ease of use and a good agreement with experimental data, however, have made pseudo-Voigt profiles most widely used.[18,24] Pseudo-Voigt functions are a linear combination (instead of a convolution) of a Gaussian and a Lorentzian, both with the same full width at half maximum. The fraction that comes from the Lorentzian function is given by a mixing parameter η. This then suggests a simple estimation of the relative contributions from different types of disorder, as a supplement to first-order methods used to estimate average size contributions (i.e., Scherrer's formula). The normalized pseudo-Voigt profiles for a range of mixing parameters are shown in Fig. 7(a), which shows how the shape changes with η.

One can then consider using the trend in the values for the mixing parameter for a family of $m(hkl)$ peaks to draw conclusions about the relative contributions of size, paracrystallinity, and lattice-spacing fluctuations to peak broadening. As a starting point, the relationship between the mixing parameter
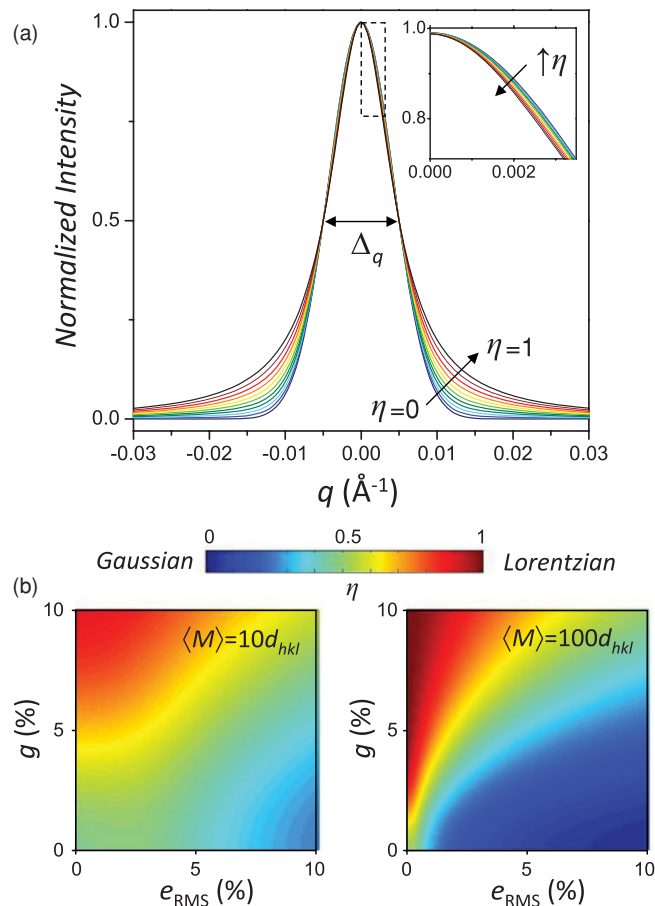
and the different WA-related variables is explored. This is done by fitting the Fourier transform of a pseudo-Voigt peak directly to the WA function, $A_m(n)$ [Eq. (10)].

For a given column length, the dependence of η vs (g, e_{rms}) is shown in Fig. 7(b). This is only done for the $m = 1$ (first-order) peak because the $A_m(n)$ coefficients for $m \neq 1$ are equivalent to those of the $m = 1$ peak but with rescaled disorder terms $g' = mg, e'_{rms} = me_{rms}$. Values for η can then be extracted from this map by selecting the (g, e_{rms}) pairs or a range of values by using the confidence intervals for (g, e_{rms}) to define an area. Each η map considers one average column length.

To show the potential for this analysis, we use the three data sets in this work. We obtain an approximate column length using the Scherrer formula and then obtain an η map [e.g., Fig. 7(b)]. We subsequently estimate pseudo-Voigt parameters for peaks with the g and e_{rms} obtained from the WA full fit. Figure 8 shows the agreement between the mixing parameter derived from the η maps and those from pseudo-Voigt fits of the isolated diffraction peaks. The shaded regions shown in Fig. 8(b) are the range of η that is obtained from the maps using g and e_{rms} values within a percent of the WA full-fit results. While the peak-fit determined values for the mixing parameter [symbols in Fig. 8(b)] differ slightly from those predicted by the η maps, these discrepancies can be explained by errors associated with uncertainty in the crystallite size (determined using the Scherrer equation), as well as by the fact that this was done for a single column length and not a distribution. Nevertheless, the approximate value and general trend of mixing parameter with diffraction order are predicted correctly.

The ultimate goal is, however, to start with the diffraction pattern and fit a background plus a series of pseudo-Voigt peaks and, without performing the complete Warren-Averbach analysis, to gain insight as to the disorder in the material. This is done by looking first at the trend in peak width with diffraction order [Fig. 8(a)]: an increasing width with order means that there is a disorder component, and a roughly constant peak width (as with TIPS-pentacene) means that size

FIG. 7. (Color online) Relation of pseudo-Voigt mixing parameter (η) to g and e_{rms}. (a) Depiction of pseudo-Voigt line profile in the full range of η's. $\eta = 0$ represents a Gaussian line shape, and $\eta = 1$ represents a Lorentzian. (b) η maps showing the mixing parameter associated with various g and e_{rms} values for an average column length of 10 repeat units (left) and 100 repeat units (right). For each of the panels in (b), the top left corner tends to $\eta = 1$ and the bottom right corner tends to $\eta = 0$.
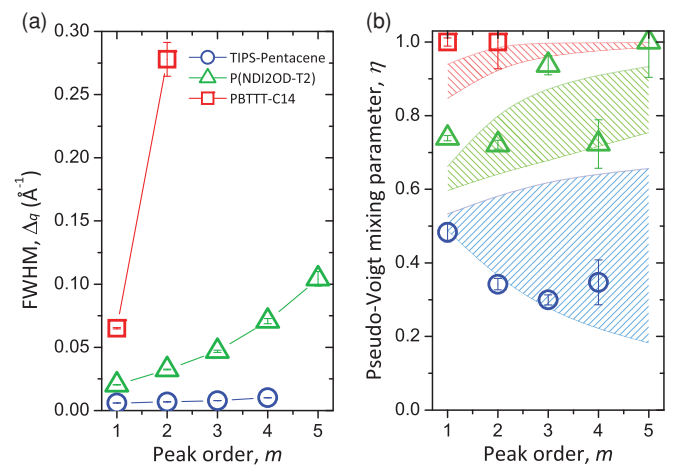

FIG. 8. (Color online) Peak parameters determined from isolated peaks of TIPS-Pn (blue circle), P(NDI2OD-T2) (green triangle), and PBTTT (red square). (a) Peak width, Δ_q, as a function of peak order (the lines are guides to the eye). (b) Pseudo-Voigt mixing parameter, η, as a function of peak order. The predictions of η from maps such as those in Fig. 7 are shown as shaded areas.

effects dominate. Assuming a varying width with diffraction order, we now turn to the η vs m trend [Fig. 8(b)]. Relatively constant values of η close to unity point to a g-dominated regime (Lorentzian), and if η is slowly varying and close to zero (Gaussian), then e_{rms} dominates the peak shape with little effect from size or paracrystallinity. If η is not near 0 or 1, both paracrystallinity and lattice-parameter fluctuations are important and the diffraction-order trends become more important. A decreasing $\eta(m)$ indicates an increasing Gaussian component, thus a larger e_{rms}; an increasing η vs m indicates a stronger paracrystalline disorder (g). Relatively constant values of η near 0.5 suggest comparable contributions from both g and e_{rms}, and a more detailed study must be performed to determine the exact contributions.

The magnitudes and $\eta(m)$ dependencies are reflected in our data sets, where at least some order-dependent broadening is observed in all materials [see Fig. 2(b) and insets in Figs. 3 and 4]. TIPS-pentacene has an $\eta < 0.5$ and a decreasing trend, characteristic of its highly crystalline behavior (very low g). P(NDI2OD-T2) illustrates a competition between non-negligible effects of paracrystallinity and lattice-spacing fluctuations with its relatively constant $\eta \sim 0.75$ values—note the large fluctuation in mixing parameter for the $m = 4$ and 5 peaks, which is due to the low intensities of these peaks. As for the PBTTT ribbon phase, a strong paracrystallinity is again observed in its $\eta \sim 1$ values for $m = 1$ and 2.

We have shown that the peak full width and mixing parameter, especially when multiple orders of diffraction are accessible, provide a relative assessment of the crystallite size, paracrystallinity, and lattice-parameter fluctuation. Differences in the line-shape pseudo-Voigt parameters can provide meaningful insight into the degree and nature of disorder.

VI. CONCLUSIONS

The study of intracrystalline lattice disorder is important for understanding electronic and optical processes in organic semiconductors. Size and disorder effects in these materials are particularly significant because van der Waals bonding dominates the crystalline structure.

In this work we adapt the Warren-Averbach technique to analyze diffraction line shapes. We incorporate careful error propagation and weighted fitting to improve results and determine conservative confidence intervals for the obtained parameters for data sets of two high-performing polymeric semiconductors, P(NDI2OD-T2) and PBTTT, and a solution-processable small molecule semiconductor, TIPS-pentacene. We focus on one class of materials, but show a range of different disorder regimes to demonstrate the wide applicability and robustness of our approach. We further discuss the incorporation of different column-length distributions and their effect on the fits. We show that as paracrystalline disorder becomes large (as high as 7.3% in the cases of PBTTT ribbon phase π-stacking) the determination of crystallite size by scattering techniques is unreliable. To further address the relation between size terms and coherence length, a disorder-induced coherence length for paracrystalline materials is presented. Furthermore, we suggest that trends in the pseudo-Voigt parameters of the diffraction peaks can be used to extract

preliminary estimates of the magnitude and type of distortion in paracrystalline materials. While we only focus on materials within the realm of organic semiconductors, we emphasize that the nature of the analyses presented here is general and valid for various spacing length scales (e.g., block copolymers, photonic crystals, and metamaterials) provided the diffraction peaks can be fully resolved.

APPENDIX A: ERROR PROPAGATION

In this Appendix, a detailed discussion on the propagation of errors is provided. While the preliminary operations and definitions used below are explored in Ref. 68, we include them for completeness. Starting from basic concepts, a general framework for the propagation of errors in the different data analysis processes will be described.

A simple way to propagate uncertainty in measured variables is by keeping track of their variance,

$$\text{var}(x) = \sigma_x^2 = \langle (x - \langle x \rangle)^2 \rangle = \langle x^2 \rangle - \langle x \rangle^2. \quad \text{(A1)}$$

When there are several inputs (x_i) and outputs (y_i) to a given operation, their variance can be expressed as a vector,

$$\sigma_{y_j}^2 = \sum_i \sigma_{x_i}^2 \left(\frac{\partial y_j}{\partial x_i} \right)^2. \quad \text{(A2)}$$

However, the outputs can be correlated even if the inputs are not. For this we need to introduce the concept of covariance,

$$\text{cov}(A, B) = \sigma_{AB}^2 = \langle AB \rangle - \langle A \rangle \langle B \rangle, \quad \text{(A3)}$$

and notice that $\text{cov}(A,B) = \text{cov}(B,A)$. The next step in the generalization of Eq. (A2) is

$$\sigma_{y_j y_l}^2 = \sum_i \sigma_{x_i}^2 \frac{\partial y_j}{\partial x_i} \frac{\partial y_l}{\partial x_i}, \quad \text{(A4)}$$

which has the form of a matrix: the variance-covariance matrix, C_{jl} (or covariance matrix for short). This is a symmetric matrix with the variance of each variable in the main diagonal, and the off-diagonal elements are the covariance terms. With this, the general way of propagating the covariance in the inputs $\{x\}$ to the outputs $\{y\}$ of a given step in the process is

$$C_{ij}^{\text{out}} = \frac{\partial y_i}{\partial x_k} C_{ks}^{\text{in}} \frac{\partial y_s}{\partial x_j}. \quad \text{(A5)}$$

This can then be expressed in matrix notation as

$$C^{\text{out}} = \left[\frac{\partial y}{\partial x}\right] C^{\text{in}} \left[\frac{\partial y}{\partial x}\right]^T, \tag{A6}$$

where $[\ ]^T$ denotes the transpose operation. This will be important in order to facilitate the calculations in the following sections, as well as the practical implementation of the routine.

1. Uncertainty in the data

The first task is to determine the error in the data, which are the counts in a detector (Y_{det}) normalized to the incidence beam ion chamber (Φ_o) and any predetector absorber with transmittance T_{abs}. The error is given by the Poisson statistics in the detector counts $\sigma_y^2 = y$. Thus, the error in our measured diffracted intensity is

$$\sigma_I = \frac{\sqrt{Y_{\text{det}}}}{T_{\text{abs}}\Phi_o}. \tag{A7}$$

The error in the scattering vector q comes from sample/diffractometer misalignment and a small but finite acceptance angle of the collimator. These errors are small, constant, and independent of q. With this reasoning, and because the routine described here does not consider absolute peak position, errors in the independent variable q are ignored.

2. Least-squares fitting routines

Consider an N-point data series $\{(x_1, y_1), \ldots, (x_N, y_N)\}$ to which we want to fit a function $f(x) = f(x;\boldsymbol{p})$, where the fitting function has a set of n parameters $\boldsymbol{p} = \{p_1, p_2, \ldots, p_n\}$. As determined in Eq. (A5), we need to calculate the following derivative of the performed operations, for which we use the chain rule

$$\frac{\partial f_j}{\partial y_i} = \sum_k \frac{\partial f_j}{\partial p_k} \frac{\partial p_k}{\partial y_i}. \tag{A8}$$

We recognize the first term in the sum as the Jacobian matrix

$$\frac{\partial f_j}{\partial p_k} = J = \begin{bmatrix} \frac{\partial f(x_1;\vec{p})}{\partial p_1} & \cdots & \frac{\partial f(x_N;\vec{p})}{\partial p_1} \\ \vdots & \ddots & \vdots \\ \frac{\partial f(x_1;\vec{p})}{\partial p_n} & \cdots & \frac{\partial f(x_N;\vec{p})}{\partial p_n} \end{bmatrix}, \tag{A9}$$

which is obtained as an output from most of the commonly used fitting routines. The $\partial p/\partial y$ term in Eq. (A8), however, requires more careful consideration. Nonweighted least-squares fitting routines solve the set of equations

$$\frac{\partial}{\partial p_i} \left\{ \sum_j [y_j - f(x_j;\vec{p})]^2 \right\} = 0, \tag{A10}$$

with a solution $\boldsymbol{p} = \boldsymbol{p}_o$. Allowing for variations in the initial data $\{y\} \to \{y\} + \{\delta y\}$, causes a change in the solution $\{p\} \to \{p\} + \{\delta p\}$. Using this, the new fitting function can be approximated as

$$f(x;\vec{p}_o + \delta\vec{p}) \approx f(x;\vec{p}_o) + \left.\frac{\partial f(x;\vec{p})}{\partial \vec{p}}\right|_{\vec{p}_o} \cdot \delta\vec{p}. \tag{A11}$$

Inserting Eq. (A11) into Eq. (A10), it can be shown that

$$\frac{\partial p_i}{\partial y_j} = (JJ^T)^{-1} J. \tag{A12}$$

It is important to notice that the Jacobian is not a square matrix and thus lacks an inverse. The product JJ^T, on the other hand, is invertible. Finally, we can write

$$\frac{\partial f_j}{\partial y_i} = J(JJ^T)^{-1} J \tag{A13}$$

and use this along with the covariance matrix for error propagation as described earlier. Note that a common mistake is to include variables that play little to no role in the fits, which then results in nearly-zero elements in the Jacobian and a badly scaled matrix. This is useful for identifying unnecessary fitting parameters.

One of the assumptions in a nonweighted least-squares regression is that each data point provides equally precise information (the error bars are all equal). By keeping track of the covariance in the data at each step of the data analysis, however, one realizes that for peaks with appreciable noise the higher-frequency components suffer from large error, as expected. A way to maximize the efficiency of the fitting-parameter estimation is to use a weighting function for the residues as part of the least-squares fitting. Optimal results, minimizing the uncertainty in the fitted parameters, are obtained when the weights are inversely proportional to the variance of each data point,

$$\frac{\partial}{\partial p_i} \left[\sum_j \left(\frac{y_j - f(x_j;\vec{p})}{\sigma_j} \right)^2 \right] = 0, \tag{A14}$$

which allows us to transform to the variables

$$\hat{y}_j = \frac{y_j}{\sigma_j}, \qquad \hat{f}(x_j;\vec{p}) = \frac{f(x_j;\vec{p})}{\sigma_j} \tag{A15}$$

and use the same formalism as for a nonweighted fitting routine. In the last step, we convert back to the original variables $y, f(x,p)$. For this we take into account that

$$\begin{aligned} \frac{\partial p_s}{\partial y_i} &= \frac{\partial p_s}{\partial \hat{y}_k} \frac{\partial \hat{y}_k}{\partial y_i} = \frac{\partial p_s}{\partial \hat{y}_i} \frac{1}{\sigma_i}, \\ \frac{\partial f_j}{\partial p_s} &= \frac{\partial f_j}{\partial \hat{f}_k} \frac{\partial \hat{f}_k}{\partial p_s} = \sigma_j \frac{\partial \hat{f}_j}{\partial p_s} \end{aligned} \tag{A16}$$

and substitute accordingly into Eqs. (A8), (A12), and (A13).

3. Background subtraction (peak isolation)

In order to obtain the isolated intensity of each diffraction order, contributions from background scattering and adjacent peaks must be subtracted from the raw data. This retains the experimental data for the isolated peak of interest (any shape asymmetries are retained). The isolated peak will then be $y^{\text{peak}} = y^{\text{raw}} - f^{\text{subs}}$, where f^{subs} is a function representing all scattered intensity not attributed to the peak in question. There will be some cross terms in the covariance matrix of the isolated peak,

$$\begin{aligned} C_{ij}^{\text{peak}} &= \text{cov}\left(y_i^{\text{raw}} - f_i^{\text{subs}}, y_j^{\text{raw}} - f_j^{\text{subs}}\right) \\ &= \text{cov}\left(y_i^{\text{raw}}, y_j^{\text{raw}}\right) + \text{cov}\left(f_i^{\text{subs}}, f_j^{\text{subs}}\right) \\ &\quad + \text{cov}\left(y_i^{\text{raw}}, -f_j^{\text{subs}}\right) + \text{cov}\left(-f_i^{\text{subs}}, y_j^{\text{raw}}\right). \end{aligned} \tag{A17}$$

The first term in Eq. (A17) is the covariance matrix of the inputs C_{ij}^{raw}, the second is the covariance matrix of the values predicted with the f^{subs} function, C_{ij}^{subs},

$$C^{\text{subs}} = \left[\frac{\partial f^{\text{subs}}}{\partial y^{\text{raw}}}\right] C^{\text{raw}} \left[\frac{\partial f^{\text{subs}}}{\partial y^{\text{raw}}}\right]^T, \qquad (A18)$$

and due to the symmetry of the covariance matrices we see that the fourth term in Eq. (A17) is the transpose of the third,

$$\begin{aligned}
\text{cov}\left(y_i^{\text{raw}}, -f_j^{\text{subs}}\right) &= \left\langle -y_i^{\text{raw}} f_j^{\text{subs}}\right\rangle - \left\langle y_i^{\text{raw}}\right\rangle\left\langle -f_j^{\text{subs}}\right\rangle \\
&= -C_{jj}^{\text{raw}}\frac{\partial f_i^{\text{subs}}}{\partial y_j^{\text{raw}}} = -C^{\text{raw}}\left[\frac{\partial f^{\text{subs}}}{\partial y^{\text{raw}}}\right].
\end{aligned}$$
$$(A19)$$

Now we need to calculate

$$\frac{\partial f_i^{\text{subs}}}{\partial y_j^{\text{raw}}} = \frac{\partial f_i^{\text{subs}}}{\partial p_k} \cdot \frac{\partial p_k}{\partial y_j^{\text{raw}}}, \qquad (A20)$$

taking into account that the background parameters p_k come from a multistep fitting routine. Note that the function f^{subs} does not directly depend on the parameters of the peak in question.

4. Two-step fitting routines

The way in which error is propagated must be revised when considering fit refinement within a reduced range of data, for example, a small window around one peak. This is because only a subset of parameters is fit, while keeping the rest constant. Dividing the global fitting variables $\boldsymbol{p}$ into two subsets, $\boldsymbol{\alpha}$ and $\boldsymbol{\beta}$, where the values for $\boldsymbol{\alpha}$ are determined in the first fitting step and the values for $\boldsymbol{\beta}$ are determined in the second step. For the subset $\boldsymbol{\alpha}$, the derivatives with respect to variations in the data are the same as described in Sec. A 1, but only taking those rows in the Jacobian that pertain to the parameters belonging to $\boldsymbol{\alpha}$. For $\boldsymbol{\beta}$, however, we need to account for the effect of the variables that have already been fixed ($\boldsymbol{\alpha}$) but still have errors,

$$\begin{aligned}
\frac{\partial \boldsymbol{\beta}}{\partial y} &= \left(\frac{\partial \boldsymbol{\beta}}{\partial y}\right)_\alpha + \frac{\partial \boldsymbol{\beta}}{\partial \alpha}\frac{\partial \alpha}{\partial y} \\
&= \left[\left(J_f J_f^T\right)^{-1} J_f\right] + \frac{\partial \boldsymbol{\beta}}{\partial \alpha}\left[\left(J_c J_c^T\right)^{-1} J_c\right]_{p\in\alpha}, \quad (A21)
\end{aligned}$$

where J_f is the Jacobian of the fitting function (derivatives with respect to $\boldsymbol{\beta}$ only, since $\boldsymbol{\alpha}$ is constant here) evaluated at the solution obtained in the second fitting step. To obtain $\partial\boldsymbol{\beta}/\partial\boldsymbol{\alpha}$ we carry out a calculation similar to that shown in Sec. A 1 for $\partial p_i/\partial y_j$,

$$\frac{\partial \boldsymbol{\beta}}{\partial \alpha} = -\left(J_f J_f^T\right)^{-1} J_f D^T, \qquad (A22)$$

where D is a matrix of derivatives of the function f with respect to those "constant" parameters from the first fitting step.

5. Data interpolation

Interpolation of data is important in order to use the efficient numerical Fourier-transform algorithms (which require that the data are symmetric and exactly centered on the peak) and it is unlikely that our points fall exactly on the peak

centers and extend symmetrically to the peak wings. Thus, data interpolation is used to shift our data points so that there is a value at $q = q_{\text{center}}$ for the peak in question and take a symmetric range of data both to lower and higher q values.

A high point density should be obtained from the diffraction experiments and not fictitiously created by excessive interpolation. Linear interpolation is sufficient and is simple to implement,

$$\tilde{y}_i = y_i + \left(\frac{y_{i+1} - y_i}{\Delta x}\right)\varepsilon\Delta x = (1-\varepsilon)y_i + \varepsilon y_{i+1}, \quad (A23)$$

where ε is the fraction of the point spacing that we need to shift, and we should notice that the interpolated data $\tilde{y}$ has one less point than the original, y. Thus, the derivative matrix will not be square, with the only nonzero elements being $(1-\varepsilon)$ on the main diagonal and ε in the diagonal above it.

6. Discrete Fourier transforms

This part of the discussion will be focused on the fast-Fourier-transform (FFT) algorithm implemented in the commercial package MATLAB (R2010a) but can easily be extended to other versions of the algorithm. The Fourier transform $Y = \mathcal{F}(y)$ of an $(N + 1)$ element vector containing the data, y, is given by

$$Y_k = \sum_{j=1}^{N+1} y_j \exp\left[-\frac{i2\pi}{N+1}(j-1)(k-1)\right]. \quad (A24)$$

The x-axis associated with this vector is determined by the Nyquist-Shannon theorem. Since the diffraction data points have no imaginary components, the real-valued coefficients of the cosine series are

$$A_m(k) = \sum_{j=1}^{N+1} y_j \cos\left[\frac{2\pi}{N+1}(j-1)(k-1)\right]. \quad (A25)$$

The errors in this step of the process originate from the uncertainty in the values for y_j and on the peak center. Errors in the y_j values affect mostly the higher-frequency components, except in pathological cases. An incorrect choice of the peak center will lead to asymmetry in the peak and result in erroneous values for the Fourier coefficients. The first part of the error propagation can be calculated using the covariance matrix approach with the derivatives of the process expressed as

$$\frac{\partial A_m(k)}{\partial y_j} = \cos\left[\frac{2\pi}{N+1}(j-1)(k-1)\right]. \qquad (A26)$$

The second source of error affects the proper indexing of the data points and can be written as

$$\begin{aligned}
\frac{\partial A_m(k)}{\partial j} = \sum_{j=1}^{N+1} &\left(\frac{\partial y_j}{\partial j}\cos\left[\frac{2\pi}{N+1}(j-1)(k-1)\right]\right. \\
&\left.+ \frac{2\pi}{N+1}(k-1)y_j \sin\left[\frac{2\pi}{N+1}(j-1)(k-1)\right]\right).
\end{aligned}$$
$$(A27)$$

The uncertainty in the point indexing is the uncertainty in the peak center (σ_{q_o}) divided by the point spacing (Δq). This means we need to add the following elements

along the diagonal of the covariance matrix of the Fourier components:

$$\frac{\sigma_{q_o}^2}{(\Delta q)^2}\left(\frac{\partial A_m(k)}{\partial j}\right)^2. \tag{A28}$$

The derivative of y_j with respect to the index j, $\partial y_j/\partial j$, can be calculated by padding each side of it with one zero and using an average of the forward- and backward-difference approximation of the first derivative.

7. Normalization and hook effect correction

Before performing the fit to the Warren-Averbach function, we need to normalize the Fourier spectrum of each peak so that the zero frequency component of the Fourier spectrum is equal to unity. The simplest case is when we use a regular division by the $A_m(1)$ element, where we are labeling the elements by a counting index $k = 1,2,3,\ldots$,

$$\tilde{A}_m(k) = \frac{A_m(k)}{A_m(1)}, \tag{A29}$$

and the derivative matrix is

$$\frac{\partial \tilde{A}_m(k)}{\partial A_m(j)} = \frac{1}{A_m(1)}\delta_{kj} - A_m(k)\left(\frac{1}{A_m(1)}\right)^2\delta_{1j}. \tag{A30}$$

The first term is a scalar multiplying the identity matrix, and the second is a matrix where the only nonzero elements are in the first column and the kth row has the element $A_m(k)[A_m(1)]^{-2}$. This makes the resulting covariance matrix $C_{ij} \neq 0$, in general, only for $i,j \neq 1$. Since we define $\tilde{A}_m(1) = 1$, any variance or covariance terms involving it are zero.

Sometimes the lower-frequency components in the Fourier spectrum have an unphysical negative curvature, showing what is called the "hook effect." If this is not accounted for, the WA fitting parameters will be incorrect. A common way to correct for this is to fit a line to the first few Fourier components, extrapolate to $k = 1$, and normalize by this value instead of the $A_m(1)$ as before. If we use the range $\nu \leqslant k \leqslant \chi$ for our linear fit, the value used for normalizing would be

$$A'_o = \frac{\langle k-1\rangle\langle(k-1)A_k\rangle - \langle A_k\rangle\langle(k-1)^2\rangle}{\langle k-1\rangle^2 - \langle(k-1)^2\rangle}, \tag{A31}$$

where the angle brackets denote averages. Similarly to that of the regular normalization, we have a matrix of derivatives

$$\frac{\partial \tilde{A}_m(k)}{\partial A_m(j)}$$

$$= \frac{1}{A'_o(1)}\delta_{kj} - 2A_m(k)\left(\frac{1}{A'_o}\right)^2$$

$$\times\left[\frac{2[\nu^2 + \chi^2 + \nu\chi - 3(\chi - \nu - 1)] - 3j(\chi + \nu - 2)}{(\chi - \nu)^3}\right]$$

$$\times[H(k-\nu) - H(k-\chi)], \tag{A32}$$

where the second term uses the Heaviside step function $H(k)$ to guarantee that it is only nonzero if $\nu \leqslant k \leqslant \chi$.

8. Weighted Warren-Averbach fits

Once all the Fourier coefficients and their respective covariance matrices have been calculated, the WA fitting step can be performed. The covariance matrix of the obtained WA parameters $\{P_i\}$ can be calculated in the same way described before for the least-squares fits, with

$$\frac{\partial P}{\partial A} = (J_{\text{WA}}J_{\text{WA}}^T)^{-1}J_{\text{WA}} \tag{A33}$$

from the Jacobian, J_{WA}, of the WA fitting function, so that

$$C_{\text{WA}} = \left[\frac{\partial P}{\partial A}\right]C_{\text{FFTs}}\left[\frac{\partial P}{\partial A}\right]^T, \tag{A34}$$

where C_{FFTs} is a block-diagonal matrix made up of all the covariance matrices for the individual peak Fourier coefficients. The square root of the diagonal of this matrix contains the error for the desired parameters (M, w, g, e_{rms}).

The process described here deals with the propagation of random errors in the measurements through each step in the data manipulation process. It should be noted that even when we fit a model function $f(x)$ to a precisely known data set $\{X,Y\}$, the determined parameters for $f(x)$ have some error due to a less than perfect description of the data by $f(x)$. A common way to account for this lack of correspondence between a model fitting function and the data is to use the residues to estimate the variance in the sampled data. This estimator is then assigned as the uncertainty to each fitted point and the usual covariance matrix formalism to propagate such errors to the results. We use a hybrid of both approaches, calculating the variance estimator after each operation, and substituting the values in the diagonal of the corresponding covariance matrix if they are lower than the estimator. This would always consider the worst case scenario for error propagation.

As a final remark, it is important to note that errors are compounded with every operation, so streamlining the algorithm and taking out unnecessary steps is helpful and should be done whenever possible.

APPENDIX B: X-RAY COHERENCE LENGTH IN STRONGLY DISORDERED SAMPLES

In the following we arrive at an expression to calculate the disorder-associated x-ray coherence length as a result of cumulative lattice disorder, using an idealized Warren-Averbach profile and the Scherrer equation. For this we consider Eq. (10) and notice that when the disorder is small, the Fourier components become negligible for $n > M/d_{hkl}$. However, when the disorder terms dominate (are sufficiently large), the exponential term will control the shape of $A_m(n)$ and the Fourier components will become negligible for $n < M/d_{hkl}$.

To determine the disorder-associated coherence length ξ purely induced by disorder, we first calculate the breadth of a peak described by an infinite-sized crystallite with the only broadening mechanisms being paracrystalline disorder (g) and lattice-parameter fluctuations (e_{rms}). Then, we use this breadth and the Scherrer expression to calculate ξ. This is equivalent to

the coherence length determined from the distance over which the lattice loses crystallographic coherence (waves scatter π out of phase). In this case, the Fourier spectrum of the first-order ($m = 1$) reflection is given by

$$A(n) = A^D(n) = \exp\left[-2\pi^2\left(ng^2 + n^2 e_{\text{rms}}^2\right)\right]. \quad (B1)$$

If we now express this in terms of position $x = nd_{hkl}$ instead of unit cells, we see that the peak in q space will be given by

$$
\begin{aligned}
I(q) &\propto \int_{-\infty}^{\infty} A_m(x,q)\exp[iqx]\,dx \\
&= \int_{-\infty}^{\infty} \exp\left[-2\pi^2\left(\frac{|x|}{d_{hkl}}g^2 + \frac{x^2}{d_{hkl}^2}e_{\text{rms}}^2\right)\right]\exp[iqx]\,dx.
\end{aligned}
\quad (B2)
$$

This will result in a Voigt profile, with the full width at half maximum of the Lorentzian component

$$\Delta_{\text{Lorentz}} = \frac{4\pi^2 g^2}{d_{hkl}} \quad (B3)$$

and that of the Gaussian component

$$\Delta_{\text{Gauss}} = 2\sqrt{2\,\ln(2)}\frac{4\pi^2 e_{\text{rms}}}{d_{hkl}}. \quad (B4)$$

The full width at half maximum (FWHM) of the complete Voigt profile can be approximated by[69]

$$
\begin{aligned}
\Delta_{\text{Voigt}} &\approx c_1\Delta_{\text{Lorentz}} + \sqrt{c_2(\Delta_{\text{Lorentz}})^2 + (\Delta_{\text{Gauss}})^2} \\
&= \frac{4\pi^2 g^2}{d_{hkl}}\left[c_1 + \sqrt{c_2 + \frac{8\,\ln(2)e_{\text{rms}}^2}{g^2}}\right],
\end{aligned}
\quad (B5)
$$

with $c_1 = 0.5346$ and $c_2 = 0.2166$. Inserting this into the Scherrer equation [Eq. (1)] one obtains

$$\xi \approx \frac{d_{hkl}}{2\pi g^2}\frac{1}{c_1 + \sqrt{c_2 + \frac{8\,\ln(2)e_{\text{rms}}^2}{g^2}}}. \quad (B6)$$

A common limiting case is that where $e_{\text{rms}} = 0$. This is relevant when considering systems where g overwhelmingly dominates. In this case, we have

$$\xi = \frac{d_{hkl}}{2\pi g^2}. \quad (B7)$$

---

[1] R. L. Snyder, J. Fiala, and H. J. Bunge, *Defect and Microstructure Analysis by Diffraction* (Oxford University Press, Oxford, 1999).

[2] A. M. Hindeleh and R. Hosemann, J. Mater. Sci. **26**, 5127 (1991).

[3] J. L. Bredas, J. P. Calbert, D. A. da Silva Filho, and J. Cornil, Proc. Natl. Acad. Sci. USA **99**, 5804 (2002).

[4] J. Rivnay, R. Noriega, J. E. Northrup, R. J. Kline, M. F. Toney, and A. Salleo, Phys. Rev. B **83**, 121306(R) (2011).

[5] B. E. Warren, *X-Ray Diffraction* (Addison-Wesley, Reading, MA, 1969).

[6] D.-M. Smilgies, J. Appl. Crystallogr. **42**, 1030 (2009).

[7] A. M. Hindeleh and R. Hosemann, J. Phys. C **21**, 4155 (1988).

[8] B. Crist and J. B. Cohen, J. Polym. Sci., Polym. Phys. Ed. **17**, 1001 (1979).

[9] H. Bradaczek, in *Defect and Microstructure Analysis by Diffraction*, edited by R. L. Snyder, J. Fiala, and H. J. Bunge (Oxford University Press, Oxford, 1999), p. 234.

[10] H. Takahashi, J. Phys. Soc. Jpn. **27**, 708 (1969).

[11] H. P. Klug and L. E. Alexander, *X-Ray Diffraction Procedures for Polycrystalline and Amorphous Materials* (Wiley, New York, 1974).

[12] J. I. Langford, in *Diffraction Analysis of the Microstructure of Materials*, edited by E. J. Mittemeijer and P. Scardi (Springer-Verlag, Berlin, 2004).

[13] P. Scardi, M. Leoni, and R. Delhez, J. Appl. Crystallogr. **37**, 381 (2004).

[14] W. H. Hall, Proc. Phys. Soc. London, Sect. A **62**, 741 (1949).

[15] G. K. Williamson and W. H. Hall, Acta Metall. **1**, 22 (1953).

[16] B. E. Warren and B. L. Averbach, J. Appl. Phys. **21**, 595 (1950).

[17] B. E. Warren and B. L. Averbach, J. Appl. Phys. **23**, 497 (1952).

[18] T. J. Prosa, J. Moulton, A. J. Heeger, and M. J. Winokur, Macromolecules **32**, 4000 (1999).

[19] I. Lucks, P. Lamparter, and E. J. Mittemeijer, J. Appl. Crystallogr. **37**, 300 (2004).

[20] L. Bimbault, K. F. Badawi, P. Goudeau, V. Branger, and N. Durand, Thin Solid Films **275**, 40 (1996).

[21] T. Ungar and A. Borbely, Appl. Phys. Lett. **69**, 3173 (1996).

[22] T. Ungár, S. Ott, P. G. Sanders, A. Borbély, and J. R. Weertman, Acta Mater. **46**, 3693 (1998).

[23] J. G. M. van Berkum, R. Delhez, T. H. de Keijser, and E. J. Mittemeijer, Acta Crystallogr. A **52**, 730 (1996).

[24] D. Balzar, J. Appl. Crystallogr. **25**, 559 (1992).

[25] A. Benedetti, G. Fagherazzi, S. Enzo, and M. Battagliarin, J. Appl. Crystallogr. **21**, 543 (1988).

[26] G. Mestl, B. Herzog, R. Schloegl, and H. Knoezinger, Langmuir **11**, 3027 (1995).

[27] B. Lanson and B. Kubler, Clays and Clay Minerals **42**, 489 (1994).

[28] R. Somashekar and H. Somashekarappa, J. Appl. Crystallogr. **30**, 147 (1997).

[29] S. M. Wecker, J. B. Cohen, and T. Davidson, J. Appl. Phys. **45**, 4453 (1974).

[30] Y.-H. Ye, F. LeBlanc, A. Hache, and V.-V. Truong, Appl. Phys. Lett. **78**, 52 (2001).

[31] O. L. Pursiainen, J. J. Baumberg, H. Winkler, B. Viel, P. Spahn, and T. Ruhl, Opt. Express **15**, 9553 (2007).

[32] O. L. J. Pursiainen, J. J. Baumberg, H. Winkler, B. Viel, P. Spahn, and T. Ruhl, Adv. Mater. **20**, 1484 (2008).

[33] A. C. Arias, J. D. MacKenzie, I. McCulloch, J. Rivnay, and A. Salleo, Chem. Rev. **110**, 3 (2010).

[34] A. Facchetti, Mater. Today **10**, 28 (2007).

[35] H. Klauk, *Organic Electronics: Materials, Manufacturing and Applications* (Wiley-VCH, Weinhiem, Germany, 2006).

[36] A. Salleo, Mater. Today **10**, 38 (2007).

[37] V. Coropceanu, J. Cornil, D. A. da Silva Filho, Y. Olivier, R. Silbey, and J.-L. Bredas, Chem. Rev. **107**, 926 (2007).

[38] D. P. McMahon and A. Troisi, Chem. Phys. Chem. **11**, 2067.

[39] A. Troisi and D. L. Cheung, J. Chem. Phys. **131**, 014703 (2009).

[40] A. Troisi and G. Orlandi, Phys. Rev. Lett. **96**, 086601 (2006).

[41] Y.-F. Huang, C.-W. Chang, D.-M. Smilgies, U.-S. Jeng, A. R. Inigo, J. D. White, K.-C. Li, T.-S. Lim, T.-D. Li, H.-Y. Chen, S.-A. Chen, W.-C. Chen, and W.-S. Fann, Adv. Mater. **21**, 2988 (2009).

[42] S. Lilliu, T. Agostinelli, E. Pires, M. Hampton, J. Nelson, and J. E. Macdonald, Macromolecules **44**, 2725 (2011).

[43] Z. Chen, Y. Zheng, H. Yan, and A. Facchetti, J. Am. Chem. Soc. **131**, 8 (2008).

[44] H. Yan, Z. Chen, Y. Zheng, C. Newman, J. R. Quinn, F. Dotz, M. Kastler, and A. Facchetti, Nature (London) **457**, 679 (2009).

[45] R. Hamilton, J. Smith, S. Ogier, M. Heeney, J. E. Anthony, I. McCulloch, J. Veres, D. D. C. Bradley, and T. D. Anthopoulos, Adv. Mater. **21**, 1166 (2009).

[46] S. K. Park, T. N. Jackson, J. E. Anthony, and D. A. Mourey, Appl. Phys. Lett. **91**, 063514 (2007).

[47] T. Sakanoue and H. Sirringhaus, Nat. Mater. **9**, 736 (2010).

[48] M. L. Chabinyc, M. F. Toney, R. J. Kline, I. McCulloch, and M. Heeney, J. Am. Chem. Soc. **129**, 3226 (2007).

[49] B. H. Hamadani, D. J. Gundlach, I. McCulloch, and M. Heeney, Appl. Phys. Lett. **91**, 243512 (2007).

[50] I. McCulloch, M. Heeney, C. Bailey, K. Genevicius, I. MacDonald, M. Shkunov, D. Sparrowe, S. Tierney, R. Wagner, W. Zhang, M. L. Chabinyc, R. J. Kline, M. D. McGehee, and M. F. Toney, Nat. Mater. **5**, 328 (2006).

[51] D. M. DeLongchamp, R. J. Kline, Y. Jung, D. S. Germack, E. K. Lin, A. J. Moad, L. J. Richter, M. F. Toney, M. Heeney, and I. McCulloch, ACS Nano **3**, 780 (2009).

[52] B. J. Factor, T. P. Russell, and M. F. Toney, Macromolecules **26**, 2847 (1993).

[53] M. F. Toney, T. C. Huang, S. Brennan, and Z. Rek, J. Mater. Res. **3**, 351 (1988).

[54] J. Rivnay, M. F. Toney, Y. Zheng, I. V. Kauvar, Z. Chen, V. Wagner, A. Facchetti, and A. Salleo, Adv. Mater. **22**, 4359 (2010).

[55] J. Rivnay, R. Steyrleuthner, L. H. Jimison, A. Casadei, Z. Chen, M. F. Toney, A. Facchetti, D. Neher, and A. Salleo, Macromolecules (in press).

[56] Error in q_z is 0.007 Å^{-1} in all cases and is determined by alignment and instrumental resolution.

[57] S. C. B. Mannsfeld, M. L. Tang, and Z. Bao, Adv. Mater. **23**, 127 (2011).

[58] D. M. DeLongchamp, R. J. Kline, E. K. Lin, D. A. Fischer, L. J. Richter, L. A. Lucas, M. Heeney, I. McCulloch, and J. E. Northrup, Adv. Mater. **19**, 833 (2007).

[59] H. N. Tsao, D. Cho, J. W. Andreasen, A. Rouhanipour, D. W. Breiby, W. Pisula, and K. Müllen, Adv. Mater. **21**, 209 (2009).

[60] P. Brocorens, A. Van Vooren, M. L. Chabinyc, M. F. Toney, M. Shkunov, M. Heeney, I. McCulloch, J. Cornil, and R. Lazzaroni, Adv. Mater. **21**, 1193 (2009).

[61] M. M. Sokolowski, E. A. Marseglia, and R. H. Friend, Polymer **27**, 1714 (1986).

[62] A. Kidron, R. J. D. Angelis, and P. J. Reucroft, J. Appl. Phys. **48**, 5296 (1977).

[63] B. Marinkovic, R. R. de Avillez, A. Saavedra, and F. C. R. Assunção, Mater. Res. **4**, 71 (2001).

[64] H. Natter, M. Schmelzer, M. S. Loffler, C. E. Krill, A. Fitch, and R. Hempelmann, J. Phys. Chem. B **104**, 2467 (2000).

[65] N. C. Popa and D. Balzar, J. Appl. Crystallogr. **35**, 338 (2002).

[66] X. Zhang, S. D. Hudson, D. M. DeLongchamp, D. J. Gundlach, M. Heeney, and I. McCulloch, Adv. Funct. Mater **30**, 4098 (2010).

[67] F. Schoening, Acta Crystallogr. **18**, 975 (1965).

[68] P. R. Bevington, *Data Reduction and Error Analysis for the Physical Sciences* (McGraw-Hill, New York, 1969).

[69] J. J. Olivero and R. L. Longbothum, J. Quant. Spectrosc. Radiat. Transf. **17**, 233 (1977).